REVIEW ARTICLE

An explicit phase field material point method for modeling dynamic fracture problems

Zhixin Zeng | **Ruichen Ni** | **Xiong Zhang**🟢 | **Yan Liu**🟢

School of Aerospace Engineering, Tsinghua University, Beijing, China

Correspondence
Xiong Zhang, School of Aerospace Engineering, Tsinghua University, Beijing 100084, China.
Email: xzhang@tsinghua.edu.cn

Abstract

A novel explicit phase field material point method (ex-PFMPM) is proposed for modeling dynamic fracture problems. The rate-dependent phase field governing equation is discretized by a set of particles, and the phase field is updated by the explicit forward-difference time integration. Furthermore, the stability of the ex-PFMPM is studied. A novel explicit critical time step formula is obtained based on the system eigenvalues in one dimension and then extended to two and three dimensions. The critical time step formula takes the effect of particle position and neighboring cell interaction into consideration, and can also be used in an explicit phase field finite element method. Several numerical examples, including a dynamic crack branching, a plate with pre-existing crack under velocity boundary conditions and a three point bending problem are studied to verify the proposed ex-PFMPM. The use of the history field in the explicit method is studied, which shows that it will lead to fake phase field update and overestimation of the fracture energy in the unloading case. All of the numerical results show that the proposed ex-PFMPM has the capacity of modeling the crack initiation and propagation problems with both accuracy and efficiency.

KEYWORDS

dynamic fracture, explicit time integration, material point method, phase field method, simulation efficiency, stability analysis

1 | INTRODUCTION

The prediction of the dynamic fracture initiation and propagation is an important issue of many engineering problems. Since 19th century, many theoretical studies have been conducted in fracture mechanics. Inglis and Griffith[1] made analytical contributions to the early development of fracture, and Irwin[1] extended the Griffith's approach by developing the energy release rate criterion to analyze the growth of cracks. Although, a physical sound theory of fracture mechanism has been established nowadays, theoretical analysis of the crack growth still encounters many difficulties due to the complexity of crack patterns in engineering applications. Furthermore, the experimental analysis of crack growth is time consuming and of poor repeatability due to the inconsistent experimental samples. Therefore, the numerical simulation plays a crucial role in the study of fracture problems. In order to illustrate crack growth, various simulation models have been proposed since 1970s. The so-called element erosion technique is incorporated into the finite element method (FEM), which suffers difficulties in mass and energy conservation. Chen and Wilkins used the finite difference method (FDM)[2] to simulate fracture problems. Belyschko and his collaborators[3] employed the partition of unity principle for the

simulation of fracture problems and developed the extended finite element method (XFEM). The cohesive zone method (CZM)[4] was presented by embedding the cohesive zone at the edges or facets of the original FEM mesh.

Several meshfree methods aiming at fracture modeling have been carried out. Carpiteri et al.[5] presented an augmented Lagrangian element-free (ALEF) approach based on the construction of shape functions with a moving least-squares approximation for crack growth. Belytschko[6] put forward a technique for modeling 3D dynamically propagating cracks in elastic material by the element-free Galerkin (EFG) method. Rahman[7] proposed an interaction integral to calculate stress-intensity factors (SIFs) for mixed-mode fracture analysis with EFG, which can also be implemented in conjunction with FEM. Belytschko et al.[8] presented a simplified meshfree method for arbitrary evolving cracks called cracking-particle method, which models a crack by a discontinuous enrichment and does not require an explicit crack representation. Rabczuk et al.[9] improved the cracking-particle method, which models the cracks by splitting particles located on the opposite sides of the associated crack segments.

In recent years, the phase field fracture method,[10,11] which is based on the basic theory of Griffith elastic fracture mechanics, is widely used to simulate the propagation, branching and merging of crack. The phase field fracture method is developed within the smeared crack approach which represents crack surfaces implicitly by introducing damage variables for the degradation of materials. Therefore, the crack propagation occurs naturally without explicitly tracking the crack surface, and the cracking initiation problem can be well simulated with the use of phase field fracture model. Because of its powerful capability in crack growth simulation, the phase field fracture model has been combined with several methods (like FEM) to simulate different kinds of crack processes. Borden et al.[10] introduced a phase-field approximation to the Lagrangian method for discrete fracture problems and derived the coupling equations that govern the motion of the body and evolution of the phase-field. Aldakheel et al.[12] proposed an efficient low order virtual element method (VEM) for the phase-field modeling of isotropic brittle fracture in elastic solid structures undergoing small deformation. And plenty of works[13-15] have contributed to the further development of phase-field models for fracture in ductile materials. Borden et al.[13] presented a cubic degradation function providing a stress–strain response prior to crack initiation which approximates linear elastic behavior more accurately, and introduced a yield surface degradation function for the plastic softening mechanism to correct the nonphysical elastic deformation after crack initiation. Miehe et al.[15] extended the developed continuum phase field models from brittle fracture to ductile fracture coupled with thermo-plasticity at finite strain. Furthermore, the anisotropic fracture problem is also studied based on the phase field fracture model. A variational phase-field model for strongly anisotropic fracture was presented,[16] which resorts to the extended Cahn–Hilliard framework proposed in the context of crystal growth. A crack phase-field model was extended to capture anisotropic fracture for soft matter by an anisotropic volume-specific crack surface function and a rate-dependent formulation of the phase-field evolution.[17] However, most of the above mentioned works update the phase field with implicit time integration which leads to low computational efficiency.

In order to overcome the shortcomings of phase field with implicit time integration, an explicit phase field governing equation based on three fields was given by Miehe et al.[18] In the explicit phase field theory, the phase field can be updated with the forward-difference method for time integration. Therefore, the explicit algorithm can circumvent the difficulty of convergence in implicit form and gain great computational efficiency. Ren et al.[19] proposed an explicit phase field model for dynamic brittle fracture, in which the mechanical field is integrated with a Verlet-velocity scheme and the phase field is updated with sub-steps at each step. In their work, the phase field modulus is used, rather than the conventional phase field viscosity. Wang et al.[20] derived the driving force of phase field evolution based on the Mohr–Coulomb criterion for rock and other materials with shear frictional characteristics and developed a three-dimensional explicit parallel phase field model with the use of phase field viscosity. Ziaei et al.[21] developed a massively parallel algorithm on the graphical processing unit and designed a time adaptivity strategy to account for the decreasing critical time step during the evolution of the fields. However, the choice of the critical time step in the explicit phase field theory is still an unsolved problem. The widely used estimated formula[20] ignores the effect of the strain energy on the critical time step and may severely overestimate the critical time step, which will lead to instability during the simulation.

The material point method (MPM)[22,23] is an extension of the particle-in-cell (PIC) method. In the MPM scheme,[23] a continuum body is discretized into a set of particles which carries all the state variables moving through a predefined Eulerian background grid. The momentum equation is first solved on the background grid, and then the solution is mapped to the particles to update their state variables. The deformed background grid can be discarded at the end of every time step, and the initial regular mesh is used in next time step. The MPM combines the Lagrangian description and Eulerian description, which makes MPM have relatively natural contact algorithm and great efficiency in simulating large deformation problems.[22,23] Many efforts have been made in MPM to simulate crack problems. Nairn[24] proposed a material

point method with crack (CRAMP) which simulates a crack with multivelocity fields. Wang et al.[25] used an irregular mesh to simulate 2D mixed mode crack and introduced the surfaces of the crack by allowing the placement of two sets of nodes along the crack line. Chen et al.[26] simulated several crack problems approximately by using the collection of failure points and developed a failure criterion based on a bifurcation analysis. Liang et al.[27] introduced enriched shape functions in the material point method (EMPM) and the generalized interpolation material point method (EGIMP) to simulate crack problems and calculated fracture parameters of the crack tip such as the energy release rate and stress intensity factors. In spite of the progress that has been made in simulating crack problems, various limitations still exist. Most of the existing numerical methods of dynamic fracture require explicit description of the location and the spatial derivatives of each crack surface. And the requirement of additional relations that govern the initiation and the growth velocity and direction of the crack still can not be ignored, which makes it difficult to simulate the cracking initiation problem. To overcome the above shortcomings, a few studies have incorporated the phase field fracture model into MPM to simulate the crack growth problem. A phase field material point method (PF-MPM) has been successfully proposed by Kakouris[28] for quasi-static brittle fracture problems, and a variant accounting for anisotropy in the quasi-static regime has also been developed.[29] And Kakouris[29] further developed a novel PF-MPM for robust simulation of dynamic fracture considering the fractured contact surfaces. A grid-based adaptive technique[30] for the MPM coupled with a phase-field fracture model for brittle materials was developed to resolve the length scale in the phase-field evolution equation. However, all the above works employ the implicit phase field fracture model to couple with the MPM in the dynamic fracture problem, which leads to the low simulation efficiency and poor convergence. Wolper et al.[31] coupled MPM with a Ginzburg–Laudau type phase-field equation which is based on the explicit phase field fracture model for animating dynamic fracture. However, the gradient of the phase field at the next time step appears in the Ginzburg–Laudau type phase-field equation, which makes the method implicit, and leads to poor simulation efficiency.

More and more scholars have found that the particle distribution will heavily affect the stability of the explicit MPM,[32-34] and there are a lot of works on the stability analysis of particle methods.[35-38] Belytschko et al.[35] presented a unified stability analysis of meshless particle methods by perturbation method in one and two dimensions. Balsara[38] applied the von Neumann stability analysis method to the SPH method and Renaud[33] also applied the von Neumann stability analysis method to the discontinuous Galerkin material point method (DGMPM) for hyperbolic problems. Steffen et al.[39] proposed an optimal time step by estimating and balancing space and time errors in MPM. Berzins[40] applied the stability analysis of Spigler and Vianello[41] to MPM and derived a stable time step bound for one dimension. Ni and Zhang[42] proved that the von Neumann stability analysis method is invalid in the explicit MPM and derived the critical time step formula by solving the system generalized eigenvalue problem. The corresponding formula illustrated the effect of particle distribution and neighboring cell interaction on the stability of the standard MPM.

A novel explicit phase field material point method (ex-PFMPM) is proposed in this article to simulate the dynamic fracture problem, which updates the phase field of the computational domain by the forward-difference method. To analyze the stability of the ex-PFMPM, the effects of particle position and neighboring cell interaction on the critical time step are taken into consideration, and an explicit critical time step formula is obtained based on the system eigenvalues in one dimension and then extended to two and three dimensions. The critical time step formula can also be used in an explicit phase field finite element method. Several numerical examples of dynamic fracture problem are designed to verify the ability of ex-PFMPM in simulating crack process. And the effect of the use of history field parameters is studied.

The remainder of this article is organized as follows. Section 2 briefly reviews the theory of phase field fracture model. Section 3 presents the ex-PFMPM, and derives an explicit critical time step formula for the ex-PFMPM. Section 4 studies several numerical examples to validate the proposed method, and Section 5 draws concluding remarks.

2 | PHASE FIELD DESCRIPTION

2.1 | Diffusive crack topology of phase field crack

Different from the discrete description of the geometry of the crack, as in the XFEM, phase field is built on the idea of regularizing a sharp crack topology by a diffusive crack topology[18] as shown in Figure 1. Consider a time-dependent crack phase field $d(\boldsymbol{x}, t)$, characterizing that $d = 0$ implies the unbroken state and $d = 1$ is the fully broken state of the material at $\boldsymbol{x}$ in the current configuration. Following the idea that the crack is not a discrete phenomenon, but processed with
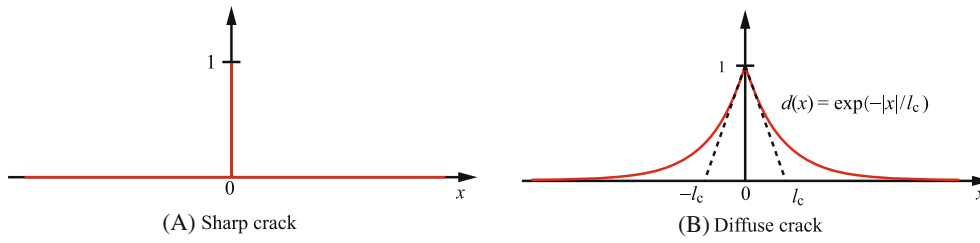
FIGURE 1 Description of cracks in 1D condition: (A) sharp crack; (B) diffuse crack.

material damage and micro-cracks aggregation, an exponential function for approximating the diffuse crack topology in 1D condition is introduced as

$$d(x) = \exp(-|x|/l_c), \tag{1}$$

where $|x|$ is the distance from the center of the crack area, l_c is a characteristic scale parameter representing the width of diffuse crack.

Therefore, a regularized crack function can be derived based on the crack surface density as

$$\Gamma_S(d) = \int_\Omega \gamma_l(d) d\Omega, \tag{2}$$

where Ω is the current configuration of the material body,

$$\gamma_l(d) = \frac{1}{2l_c} d^2 + \frac{l_c}{2} d_{,i} d_{,i},$$

is the crack surface density. Assuming a given sharp crack surface topology inside the material body at time t, the regularized crack phase field $d(\boldsymbol{x}, t)$ can be obtained by the variational principle of diffusive crack topology

$$d(\boldsymbol{x}, t) = \arg\{\inf \ \Gamma_S(d)\}, \tag{3}$$

whose Euler equations are

$$d - l_c^2 \Delta d = 0 \text{ in } \Omega, \tag{4}$$

$$\nabla d \cdot \boldsymbol{n} = 0 \text{ on } \Gamma, \tag{5}$$

where $\boldsymbol{n}$ is the outer unit normal on material boundary Γ, Δ is the Laplace operator.

2.2 | Governing equation of phase field crack

According to Griffith's theory, with the regularized crack function Equation (2), the fracture energy Ψ_f of an elastic body can be defined as

$$\Psi_f = G_c \Gamma_S = G_c \int_\Omega \left(\frac{1}{2l_c} d^2 + \frac{l_c}{2} d_{,i} d_{,i} \right) d\Omega, \tag{6}$$

where G_c is the Griffiths critical energy release rate, which is the energy required to create a unit area of fracture surface. Therefore, the total potential energy $\Psi_{pot}(u, \Gamma)$ of the material body can be written as

$$\Psi_{pot}(u, \Gamma) = \Psi_e + \Psi_f = \int_\Omega (\phi_e + \phi_f) d\Omega, \tag{7}$$

where Ψ_e is the elastic strain energy, ϕ_e is the elastic energy density, and ϕ_f is the fracture energy density. To account for the fracture-induced stress degradation only in tension, the elastic energy density is decomposed into positive and negative parts as

$$\phi_e = g_d \phi_e^+ + \phi_e^-, \tag{8}$$

where g_d is the degradation function, the positive part

$$\phi_e^+ = \frac{1}{2}\lambda\langle\varepsilon_1 + \varepsilon_2 + \varepsilon_3\rangle_+^2 + \mu(\langle\varepsilon_1\rangle_+^2 + \langle\varepsilon_2\rangle_+^2 + \langle\varepsilon_3\rangle_+^2), \tag{9}$$

is the elastic energy density due to tension, and the negative part

$$\phi_e^- = \frac{1}{2}\lambda\langle\varepsilon_1 + \varepsilon_2 + \varepsilon_3\rangle_-^2 + \mu(\langle\varepsilon_1\rangle_-^2 + \langle\varepsilon_2\rangle_-^2 + \langle\varepsilon_3\rangle_-^2). \tag{10}$$

is the elastic energy density due to compress. The λ and μ are the Lame constants, ε_i is the principal strain and $\langle\rangle_\pm$ denotes the Macaulay brackets

$$\langle A\rangle_\pm = (A \pm |A|)/2. \tag{11}$$

In phase field crack, the decrease of the elastic energy due to the degradation of the material properties need to be considered with the evolving of the crack surface. Therefore, a degradation function $g_d(d)$ that is worked on the positive part of the energy strain density is proposed to achieve the material degradation. The degradation function

$$g_d(d) = (1 - d)^2, \tag{12}$$

proposed by Miehe[18] is used here, if it is not mentioned specially. Therefore, substituting Equations (8) into (7) with the degradation, the expression for total potential energy finally assumes the form

$$\Psi_{pot}(u, \Gamma) = \int_\Omega g_d(d)\phi_e^+ d\Omega + \int_\Omega \phi_e^- d\Omega + \int_\Omega G_c \gamma_l(d, \Delta d) d\Omega. \tag{13}$$

The elastic stress field can be derived from the elastic potential as

$$\sigma_{ij} = g_d \frac{\partial \phi_e^+}{\partial \varepsilon_{ij}} + \frac{\partial \phi_e^-}{\partial \varepsilon_{ij}} = g_d \sigma_{ij}^+ + \sigma_{ij}^-, \tag{14}$$

where σ_{ij}^+ and σ_{ij}^- are the "positive" and the "negative" part of the stresses which can be written as

$$\sigma^\pm = \lambda\langle\varepsilon_1 + \varepsilon_2 + \varepsilon_3\rangle_\pm I + 2\mu\left(\langle\varepsilon_1\rangle_\pm n_1 \otimes n_1 + \langle\varepsilon_2\rangle_\pm n_2 \otimes n_2 + \langle\varepsilon_3\rangle_\pm n_3 \otimes n_3\right), \tag{15}$$

where I is the identity matrix and n_i are eigenvectors for principal strain ε_i.

Finally, taking the variation for the total potential energy with respect to the phase-field variable d and displacement u, the coupled strong form of the momentum equation and brittle-fracture phase-field formulation is established as

$$\begin{aligned}
\frac{G_c}{l_c}d + \frac{\partial g_d}{\partial d}\phi_e^+ - G_c l_c \Delta d &= 0, \\
\nabla d \cdot n &= 0 \quad \text{on } \Gamma, \\
d &= d_0 \quad \text{on } \Omega_0,
\end{aligned} \tag{16}$$

$$\begin{aligned}
\nabla \cdot (g_d \sigma^+ + \sigma^-) + b &= \rho\ddot{u}, \\
\sigma \cdot n &= t \quad \text{on } \partial\Gamma_t, \\
u &= \bar{u} \quad \text{on } \partial\Gamma_u,
\end{aligned} \tag{17}$$

where Γ_t and Γ_u denote the prescribed traction boundary and displacement boundary of Ω, respectively.

Since the initiation and propagation process of cracks is irreversible, the evolution of the phase field process should satisfy the constraints

$$d(x, t) \in [0, 1] \qquad \dot{d}(x, t) \geq 0. \tag{18}$$

The staggered solution algorithm is widely used to update the displacement field and phase field. To satisfy the evolution constraints in Equation (18) in the simulation process, the maximum positive elastic energy is taken as the history-field variable H, namely,

$$H = \max(\phi_e^+(t)) \quad \forall t > 0. \tag{19}$$

Thus, the history field satisfies the Karush–Kuhn–Tucker condition for elastic loading and unloading

$$
\begin{aligned}
H - \phi_e^+ &\geq 0, \\
\dot{H} &\geq 0, \\
\dot{H}(H - \phi_e^+) &= 0.
\end{aligned}
\tag{20}
$$

With the history-field variable replacing the positive elastic energy in the governing Equation (16), the irreversibility of the phase field is enforced. Therefore, the governing equation can be written as

$$\frac{G_c}{l_c}d + \frac{\partial g_d}{\partial d}H - G_c l_c \Delta d = 0. \tag{21}$$

2.3 | Explicit evolution of the phase field

As aforementioned, the staggered solution algorithm is widely used in the numerical application. However, a serious problem of this algorithm with the implicit phase field fracture model Equation (21) is that the convergence is not easily obtained especially for complex crack growth problems. And the simulation efficiency is quite poor due to the iteration process. Therefore, a rate-dependent phase field evolution equation[18-20] is introduced as

$$\eta \dot{d} = \langle \beta(d) - \gamma(d) \rangle_+, \tag{22}$$

where

$$\beta(d) = -\frac{\partial g_d}{\partial d} \phi_e^+,$$

is the local driving force,

$$\gamma(d) = \frac{G_c}{l_c}[d - l_c^2 \Delta d],$$

is the geometric resistance force and η denotes the phase field viscosity parameter.

The determination of the phase field viscosity parameter η is a research-worthy problem. Miche et al.[18] pointed out that η can be set as $\eta = \Delta t^2 / \epsilon$, where ϵ is another artificial regularization parameter without direct physical meaning and should be determined by the conditioning number of the system matrices. And the history field parameter in Equation (19) is used to replace the positive elastic energy to satisfy the evolution constraints in Equation (18), which leads to

$$\eta \dot{d} = \left\langle -\frac{\partial g_d}{\partial d}H - \frac{G_c}{l_c}[d - l_c^2 \Delta d] \right\rangle_+. \tag{23}$$

However, the monotonic increase of the phase field can be guaranteed directly with the Macaulay brackets $\langle \rangle_\pm$ in Equation (23). In Section 4, we will study the effects of the history field in the ex-PFMPM.

3 | EXPLICIT PHASE FIELD MATERIAL POINT METHOD

3.1 | Equilibrium discrete equations of MPM

In the MPM, a continuum body is discretized into a set of particles which carries all the physical data (phase field, velocity, momentum, density, etc.). Particles move through the Eulerian background grid during simulation, as shown in Figure 2. Therefore, the density $\rho(\boldsymbol{x})$ of the continuum body can be written as

$$\rho(\boldsymbol{x}) = \sum_{p=1}^{n_\mathrm{p}} m_p \delta(\boldsymbol{x} - \boldsymbol{x}_p), \tag{24}$$

where n_p is the number of MPM particles, m_p and $\boldsymbol{x}_p$ are the mass and position vector of particle p, respectively. The weak form of the governing Equation (17) can be expressed as

$$\int_\Omega \rho \ddot{u}_i \delta \dot{u}_i \mathrm{d}V + \int_\Omega \rho \sigma_{ij}^s \delta u_{i,j} \mathrm{d}V - \int_\Omega \rho b_i \delta u_i \mathrm{d}V - \int_{\Gamma_t} \rho t_i^s \delta u_i \mathrm{d}A = 0, \tag{25}$$

where the subscripts i and j indicate the components of the spatial variables following the Einstein convention, Ω is the material domain, Γ_t denotes the traction boundary, u_i denotes the displacement, $\sigma_{ij}^s = (g(d)\sigma_{ij}^+ + \sigma_{ij}^-)/\rho$ is the degraded specific stress, b_i and t_i^s are respectively the specific body force and traction. Substituting Equations (24) into (25) results in the discretized equation

$$\sum_{p=1}^{n_\mathrm{p}} m_p \ddot{u}_{ip} \delta u_{ip} + \sum_{p=1}^{n_\mathrm{p}} m_p \sigma_{ijp}^s \delta u_{ip,j} - \sum_{p=1}^{n_\mathrm{p}} m_p b_{ip} \delta u_{ip} - \sum_{p=1}^{n_\mathrm{p}} m_p \bar{t}_{ip}^s \delta u_{ip} h^{-1} = 0, \tag{26}$$

where the subscript p denotes the variables associated with particle p, h is the thickness of the fictitious layer used to convert the surface integral on the traction boundary Γ_t into a volume integral.

With the use of shape function N_{Ip}, the position and displacement field of particles can be approximated on the background grid as

$$x_{ip} = \sum_I N_{Ip} x_{iI}, \tag{27}$$

$$u_{ip} = \sum_I N_{Ip} u_{iI}, \tag{28}$$

where the subscript I denotes the variables associated with the grid node I. Substituting Equations (28) into (26) leads to

$$\dot{p}_{iI} = f_{iI}^{\mathrm{int}} + f_{iI}^{\mathrm{ext}} \qquad x_I \notin \Gamma_\mathrm{u}, \tag{29}$$
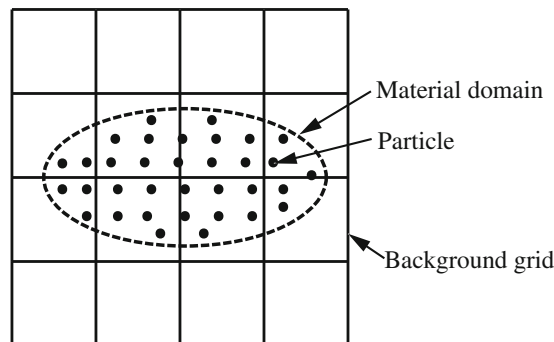

FIGURE 2 Material point method (MPM) discretation of the material domain.

where

$$p_{iI} = m_I \dot{u}_{iI}, \tag{30}$$

is the grid nodal momentum,

$$m_I = \sum_{p=1}^{n_p} m_p N_{Ip}, \tag{31}$$

is the lumped grid nodal mass,

$$f_{iI}^{\text{int}} = -\sum_{p=1}^{n_p} N_{Ip,j} \left[g_d(d_p)\sigma_{ijp}^+ + \sigma_{ijp}^- \right] \frac{m_p}{\rho_p}, \tag{32}$$

and

$$f_{iI}^{\text{ext}} = \sum_{p=1}^{n_p} m_p N_{Ip} b_{ip} + \sum_{p=1}^{n_p} N_{Ip} \bar{t}_{ip}^s h^{-1} \frac{m_p}{\rho_p}, \tag{33}$$

are the internal and external grid nodal force, respectively.

3.2 | Phase field discrete equations

The weak form of the explicit phase field governing Equation (23) can be written as

$$\int_\Omega \eta \dot{d} q \mathrm{d}v = \int_\Omega \left\{ -\frac{\partial g_d}{\partial d} H - \frac{G_c}{l_c} [d - l_c^2 \Delta d] \right\} q \mathrm{d}v, \tag{34}$$

where q is the corresponding weighting function for the phase field. Employing the integration by parts and particle quadrature, Equation (34) can be rewritten as

$$\sum_{p=1}^{n_p} \eta_p V_p \dot{d}_p q_p = \sum_{p=1}^{n_p} V_p S_p q_p - \sum_{p=1}^{n_p} G_c l_c V_p d_{,ip} q_{,ip}, \tag{35}$$

where

$$S_p = \left[-\frac{\partial g_d}{\partial d} H - \frac{G_c}{l_c} d \right]_p. \tag{36}$$

With the shape function N_{Ip}, the state variables of particle p can be interpolated from their grid nodal values, that is,

$$d_p = \sum_{I=1}^{n_g} N_{Ip} d_I, \tag{37}$$

$$q_p = \sum_{I=1}^{n_g} N_{Ip} q_I, \quad q_{p,i} = \sum_{I=1}^{n_g} N_{Ip,i} q_I, \tag{38}$$

where n_g denotes the total number of grid nodal points. Substituting Equations (37) and (38) into (35) and considering the arbitrariness of the weighting function q, the discrete weak form at grid nodes can be expressed as

$$C_I \dot{d}_I = y_I^{\text{int}} + y_I^{\text{ext}}, \tag{39}$$

where

$$C_I = \sum_{p=1}^{n_\mathrm{p}} \eta_p V_p N_{Ip}, \tag{40}$$

$$y_I^{\mathrm{ext}} = \sum_{p=1}^{n_\mathrm{p}} V_p S_p N_{Ip}, \tag{41}$$

$$y_I^{\mathrm{int}} = -G_\mathrm{c} l_\mathrm{c} \sum_{J=1}^{n_\mathrm{g}} \sum_{p=1}^{n_\mathrm{p}} V_p N_{Jp,i} N_{Ip,i} d_J. \tag{42}$$

As shown in Equation (40), a lumped viscous matrix is used in the simulation to avoid the matrix assembly.

3.3 | Stability analysis

In this section, we firstly investigate the ex-PFMPM based on the moving-mesh MPM which is referred to a MPM that is fully Lagrangian. In moving-mesh MPM, the mesh and particles keep stationary in the reference configuration and displacements of both the particles and grid nodes are kept track of. The moving-mesh MPM is actually the same as the standard FEM with the adoption of the lumped mass matrix except that the particles instead of the Gauss points serve as the quadrature points in the moving-mesh MPM. As mentioned by Ni and Zhang,[42] the effect of particle position and neighboring cell interaction on the critical time step of the standard MPM need to be taken into consideration, when conducting the stability analysis. Therefore, to get an explicit critical time step formula based on the system eigenvalues in one dimension, as shown in Figure 3, we assume that the standard MPM has uniform mesh discretization in the 1D computational domain, and the mesh size is $x_{I+1} - x_I = x_I - x_{I-1} = l$. Given that the sectional area is A, the Young's modulus is E, and the particles are numbered from 1 to $k_1 + k_2$ in sequence, the discrete governing equation of the two-cell system shown in Figure 3 can be written as

$$A\dot{D} = F - BD - KD, \tag{43}$$

where

$$D = [d_{I-1}, d_I, d_{I+1}]^\mathrm{T}, \tag{44}$$

$$A = \eta_p \begin{bmatrix} V_{I-1}^n & 0 & 0 \\ 0 & V_I^n & 0 \\ 0 & 0 & V_{I+1}^n \end{bmatrix}, \tag{45}$$

$$B = \begin{bmatrix} (2H_{I-1}^n + \dfrac{G_\mathrm{c}}{l_\mathrm{c}})V_{I-1}^n & 0 & 0 \\ 0 & (2H_I^n + \dfrac{G_\mathrm{c}}{l_\mathrm{c}})V_I^n & 0 \\ 0 & 0 & (2H_{I+1}^n + \dfrac{G_\mathrm{c}}{l_\mathrm{c}})V_{I+1}^n \end{bmatrix}, \tag{46}$$
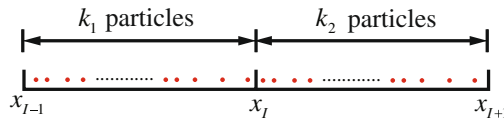

FIGURE 3 Diagram of 1D mesh and particle distribution.

and

$$
\boldsymbol{K} =
\begin{bmatrix}
K_1^n & -K_1^n & 0 \\
-K_1^n & K_1^n + K_2^n & -K_2^n \\
0 & -K_2^n & K_2^n
\end{bmatrix},
\tag{47}
$$

where

$$
K_1^n = \frac{AG_c l_c}{l^2} \sum_{p=1}^{k_1} l_p^n, \quad K_2^n = \frac{AG_c l_c}{l^2} \sum_{p=k_1+1}^{k_1+k_2} l_p^n,
\tag{48}
$$

$$
V_I^n = \sum_{p=1}^{n_p} V_p N_{Ip},
\tag{49}
$$

and l_p^n is the length of particle p in time step n. Note that $\boldsymbol{F}$ is the external load matrix, which has no influence on the system natural frequency. Therefore, we assume $\boldsymbol{F} = \boldsymbol{0}$. Based on Equation (43), with the forward-difference method in time integration, the critical time step of ex-PFMPM can be written as

$$
\Delta t_{cr} = \frac{2}{\lambda_{max}(C)},
\tag{50}
$$

where the amplification matrix C of the system is defined by

$$
\boldsymbol{C} = \boldsymbol{A}^{-1}(\boldsymbol{B} + \boldsymbol{K}) =
\begin{bmatrix}
\frac{(2H_{I-1}^n + G_c/l_c)V_{I-1}^n + K_1^n}{\eta_p V_{I-1}^n} & -\frac{K_1^n}{\eta_p V_{I-1}^n} & 0 \\
-\frac{K_1^n}{\eta_p V_I^n} & \frac{(2H_I^n + G_c/l_c)V_I^n + K_1^n + K_2^n}{\eta_p V_I^n} & -\frac{K_2^n}{\eta_p V_I^n} \\
0 & -\frac{K_2^n}{\eta_p V_{I+1}^n} & \frac{(2H_{I+1}^n + G_c/l_c)V_{I+1}^n + K_2^n}{\eta_p V_{I+1}^n}
\end{bmatrix}.
\tag{51}
$$

With the Gerschgorin's theorem, each eigenvalue $\lambda_i (i = 1, 2, 3)$ of the amplification matrix C is within the corresponding Gerschgorin set G_k, which can be written as

$$
G_k = \left\{ |g_k| < \sum_{j=1}^{3} |C_{kj}| \right\}, \quad k = 1, 2, 3.
\tag{52}
$$

Substituting Equations (51) to (52) gives the lower and upper bounds for the eigenvalues $\lambda_i (i = 1, 2, 3)$ as

$$
|\lambda_i| < \max\{a_1, a_2, a_3\},
\tag{53}
$$

where

$$
a_1 = \frac{(2H_{I-1}^n + G_c/l_c)V_{I-1}^n + 2K_1^n}{\eta_p V_{I-1}^n},
\tag{54}
$$

$$
a_2 = \frac{(2H_I^n + G_c/l_c)V_I^n + 2K_1^n + 2K_2^n}{\eta_p V_I^n},
\tag{55}
$$

$$
a_3 = \frac{(2H_{I+1}^n + G_c/l_c)V_{I+1}^n + 2K_2^n}{\eta_p V_{I+1}^n},
\tag{56}
$$

Substituting Equations (54)–(56) into the stability condition Equation (50) leads to a lower bound of the critical time step, namely,

$$
\Delta t_{cr} = \frac{2V_I^n}{(2H_I^n + G_c/l_c)V_I^n + 2K_1^n + 2K_2^n} \eta_p,
\tag{57}
$$

where K_1^n and K_2^n defined in Equation (48) will stay constant no matter how the particles are distributed in one cell, but the node volume V_I^n defined in Equation (49) will be severely influenced by the particle distribution. Therefore, the critical time step has strong correlation to the particle distribution, and it will decrease to 0 as the node volume $V_I^n \to 0$ when all the particles approach the opposite grid node of the same cell. Furthermore, the time history field H_I^n also has great influence on the critical time step, which is not considered in the literature. The critical time step will sharply decrease with the increase of the strain energy of the particle.

The computational process of the standard MPM can be divided into two steps, a Lagrangian step followed by an Eulerian step. In the Eulerian step, the mesh will be reset to its original position while the particles remain in their current positions. Ni et al.[42] stated that the Eulerian step will not make the standard MPM scheme unstable, so that the stability is determined by whether the error will be amplified in Lagrangian part. Therefore, the aforementioned stability analysis of ex-PFMPM is based on the moving mesh MPM.

However, different from the analysis in Ni and Zhang[42] for the standard MPM, the mapping and reconstruction between particles and background grids have direct influence on the stability in ex-PFMPM. The mapping and reconstruction process must be taken into consideration when calculating the critical time step. The amplification matrix C with mapping and reconstruction effects can be rewritten as

$$C = A^{-1} N_1^T N_2 (B + K), \tag{58}$$

where A, B, and K are defined in Equations (45) and (47), and

$$
N_1 = \begin{bmatrix}
V_1 N_{(I-1)\ 1} & V_1 N_{I\ 1} & 0 \\
\vdots & \vdots & \vdots \\
V_p N_{(I-1)\ p} & V_p N_{I\ p} & 0 \\
\vdots & \vdots & \vdots \\
V_{k_1} N_{(I-1)\ k_1} & V_{k_1} N_{I\ k_1} & 0 \\
0 & V_{k_1+1} N_{I\ (k_1+1)} & V_{k_1+1} N_{(I+1)\ (k_1+1)} \\
\vdots & \vdots & \vdots \\
0 & V_p N_{I\ p} & V_p N_{(I+1)\ p} \\
\vdots & \vdots & \vdots \\
0 & V_{k_1+k_2} N_{I\ (k_1+k_2)} & V_{k_1+k_2} N_{(I+1)\ (k_1+k_2)}
\end{bmatrix}, \quad
N_2 = \begin{bmatrix}
\frac{N_{(I-1)\ 1}}{V_{I-1}} & \frac{N_{I\ 1}}{V_I} & 0 \\
\vdots & \vdots & \vdots \\
\frac{N_{(I-1)\ p}}{V_{I-1}} & \frac{N_{I\ p}}{V_I} & 0 \\
\vdots & \vdots & \vdots \\
\frac{N_{(I-1)\ k_1}}{V_{I-1}} & \frac{N_{I\ k_1}}{V_I} & 0 \\
0 & \frac{N_{I\ (k_1+1)}}{V_I} & \frac{N_{(I+1)\ (k_1+1)}}{V_{I+1}} \\
\vdots & \vdots & \vdots \\
0 & \frac{N_{I\ p}}{V_I} & \frac{N_{(I+1)\ p}}{V_{I+1}} \\
\vdots & \vdots & \vdots \\
0 & \frac{N_{I\ (k_1+k_2)}}{V_I} & \frac{N_{(I+1)\ (k_1+k_2)}}{V_{I+1}}
\end{bmatrix}. \tag{59}
$$

By defining

$$
N_1^T N_2 = \begin{bmatrix}
S_{I-1}^{I-1} & S_I^{I-1} & 0 \\
S_{I-1}^I & S_I^I & S_{I+1}^I \\
0 & S_I^{I+1} & S_{I+1}^{I+1}
\end{bmatrix}, \tag{60}
$$

matrix C can be written as

$$
C = \begin{bmatrix}
S_{I-1}^{I-1} \frac{E_{I-1}+K_1^n}{\eta_p V_{I-1}^n} - S_I^{I-1} \frac{K_1^n}{\eta_p V_{I-1}^n} & -S_{I-1}^{I-1} \frac{K_1^n}{\eta_p V_{I-1}^n} + S_I^{I-1} \frac{E_I+K_1^n+K_2^n}{\eta_p V_{I-1}^n} & -S_I^{I-1} \frac{K_2^n}{\eta_p V_{I-1}^n} \\
S_{I-1}^I \frac{E_{I-1}+K_1^n}{\eta_p V_I^n} - S_I^I \frac{K_1^n}{\eta_p V_I^n} & -S_{I-1}^I \frac{K_1^n}{\eta_p V_I^n/\Delta t} + S_I^I \frac{E_I+K_1^n+K_2^n}{\eta_p V_I^n} - S_{I+1}^I \frac{K_2^n}{\eta_p V_I^n} & -S_I^I \frac{K_2^n}{\eta_p V_I^n/\Delta t} + S_{I+1}^I \frac{E_{I+1}+K_2^n}{\eta_p V_I^n} \\
-S_I^{I+1} \frac{K_2^n}{\eta_p V_{I+1}^n} & S_I^{I+1} \frac{E_I+K_1^n+K_2^n}{\eta_p V_{I+1}^n} - S_{I+1}^{I+1} \frac{K_2^n}{\eta_p V_{I+1}^n} & -S_I^{I+1} \frac{K_2^n}{\eta_p V_{I+1}^n} + S_{I+1}^{I+1} \frac{E_{I+1}+K_2^n}{\eta_p V_{I+1}^n}
\end{bmatrix}, \tag{61}
$$

where

$$E_I = (2H_I^n + G_c/l_c)V_I^n. \tag{62}$$

Substituting Equations (61) into (52) and considering the stability condition Equation (50), the critical time step Δt_{cr} with mapping and reconstruction effects is obtained as

$$\Delta t_{\mathrm{cr}} = \frac{2V_I^n}{(E_{I-1} + 2K_1^n)S_{I-1}^I + (E_I + 2K_1^n + 2K_2^n)S_I^I + (E_{I+1} + 2K_1^n)S_{I+1}^I}\eta_p. \tag{63}$$

The aforementioned analysis is based on the 1D condition. Since the background grid of the standard MPM in ex-PFMPM is always structural and orthogonal, the 1D 2-cell formula can be extended to 2D and 3D problems by decoupling the calculation of the critical time step into x-, y-, and z-direction. The critical time step of a 3D problem can be chosen as the minimum of the critical time step of each direction with the 1D 2-cell formula, that is,

$$\Delta t_{\mathrm{cr}} = \min\{\Delta t_{\mathrm{cr}}^x, \Delta t_{\mathrm{cr}}^y, \Delta t_{\mathrm{cr}}^z\}, \tag{64}$$

where Δt_{cr}^x, Δt_{cr}^y, and Δt_{cr}^z are determined by the 1D 2-cell formula of Equations (57) and (63) as

$$\Delta t_{\mathrm{cr}}^i = \frac{2V_{iI}^n}{(2H_I^n + G_{\mathrm{c}}/l_{\mathrm{c}})V_{iI}^n + 2K_{i1}^n + 2K_{i2}^n}\eta_p, \tag{65}$$

$$\Delta t_{\mathrm{cr}}^i = \frac{2V_{iI}^n}{(E_{i(I-1)} + 2K_{i1}^n)S_{I-1}^I + (E_{iI} + 2K_{i1}^n + 2K_{i2}^n)S_I^I + (E_{i(I+1)} + 2K_{i1}^n)S_{I+1}^I}\eta_p, \tag{66}$$

where the subscript i indicates the specific component of the spatial variables x, y, z. Given that there are k_1 particles and k_2 particles respectively in the two neighboring cells joint at the grid node I in x-direction, the decoupled volume V_{xI}^n, K_{x1}^n, and K_{x2}^n can be written as

$$V_{xI}^n = \sum_{p=1}^{k_1} V_p^n(1 + \xi_p)/2 + \sum_{p=k_1+1}^{k_2} V_p^n(1 - \xi_p)/2,$$

$$K_{x1}^n = \frac{G_{\mathrm{c}}l_{\mathrm{c}}}{l^2}\sum_{p=1}^{k_1} V_p^n, \tag{67}$$

$$K_{x2}^n = \frac{G_{\mathrm{c}}l_{\mathrm{c}}}{l^2}\sum_{p=k_1+1}^{k_1+k_2} V_p^n, \tag{68}$$

where r_p is the parent coordinate of particle p in x-direction. Δt_{cr}^y and Δt_{cr}^z can also be obtained in the same way with the decoupled parameter calculated by the corresponding parent coordinates s_p and t_p.

Since the orthogonal equidistant background grids are widely used in MPM, the aforementioned analysis does not consider the nonequidistant grids. However, our time step criterion can be easily generalized to nonequidistant grids by replacing Equation (48) with

$$K_1^n = \frac{AG_{\mathrm{c}}l_{\mathrm{c}}}{l_1^2}\sum_{p=1}^{k_1} l_p^n, \quad K_2^n = \frac{AG_{\mathrm{c}}l_{\mathrm{c}}}{l_2^2}\sum_{p=k_1+1}^{k_1+k_2} l_p^n, \tag{69}$$

where l_1, l_2 are the mesh size of the left and right grid of the two-cell system, respectively. And in MPM, the orthogonal background grids are commonly used due to its high efficiency in determining the parent coordinates of the material points. Besides, our MPM code employed structured mesh, so we did not derive the critical time step formula for the unstructured mesh in this work.

3.4 | Computational procedure of the explicit phase field material point method

Different from the staggered solution procedure of the coupled implicit phase field MPM, the displacement field is updated using the explicit central-difference integration and the phase field is updated using the explicit forward-difference time

integration with the use of lumped element mass/viscosity matrices in our ex-PFMPM. The following two steps are performed prior to the first time step:

1. A continuum body is discretized into a finite set of particles, which carry all physical properties (mass, volume, etc.).
2. Set the initial phase field d_p^0 of particle p based on the preset crack by

$$d_p^0 = \exp[-|x_p^0|/l_c], \tag{70}$$

where $|x_p^0|$ is the the minimum distance from particle p to the preset crack path.

For each time step, the following steps are performed:

(1) Reform the regular background mesh and reconstruct the mass, momentum and the lumped viscous dissipation parameter of background grid nodes from MPM particles by

$$m_I^k = \sum_{p=1}^{n_p} m_p N_{Ip}^k, \tag{71}$$

$$p_{iI}^{k-1/2} = \sum_{p=1}^{n_p} m_p v_{ip}^{k-1/2} N_{Ip}^k, \tag{72}$$

$$C_I^k = \sum_{p=1}^{n_p} \eta_p \frac{m_p}{\rho_p^k} N_{Ip}^k. \tag{73}$$

For fixed boundaries, impose the essential boundary condition $p_{iI}^{k-1/2} = 0$.

(2) Calculate the nodal forces of background grids by

$$f_{iI}^{\text{int},k} = -\sum_{p=1}^{n_p} N_{Ip,j}^k \sigma_{ijp}^k \frac{m_p}{\rho_p^k}, \tag{74}$$

$$f_{iI}^{\text{ext, k}} = \sum_{p=1}^{n_p} m_p N_{Ip}^k b_{ip}^k + \sum_{p=1}^{n_p} N_{Ip}^k \bar{t}_{ip}^k h^{-1} \frac{m_p}{\rho_p^k}, \tag{75}$$

$$f_{iI}^k = f_{iI}^{\text{int},k} + f_{iI}^{\text{ext},k}. \tag{76}$$

(3) Solve the momentum equation with

$$p_{iI}^{k+1/2} = p_{iI}^{k-1/2} + f_{iI}^k \Delta t^k, \tag{77}$$

and calculate the nodal crack driving force and the geometric resistance force by

$$y_I^{\text{dri, k}} = -\sum_{p=1}^{n_p} \frac{m_p}{\rho_p^k} \frac{\partial g_d}{\partial d} H_p^k N_{Ip}, \tag{78}$$

$$y_I^{\text{res, k}} = -\sum_{p=1}^{n_p} \frac{m_p}{\rho_p^k} \frac{G_c}{l_d} d_p^k N_{Ip} - \sum_{p=1}^{n_p} G_c l_d \frac{m_p}{\rho_p^k} d_{,ip}^k N_{Ip,i}, \tag{79}$$

and solve the governing Equation (39) by using the explicit forward-difference time integration

$$\Delta d_I^k = \left(y_I^{\text{dri, k}} + y_I^{\text{res, k}} \right) \Delta t^k / C_I^k. \tag{80}$$

(4) Update velocity and displacement of particles by

$$x_{ip}^{k+1} = x_{ip}^k + \Delta t^{k+1/2} \sum_{I=1}^{n_g} \frac{p_{iI}^{k+1/2} N_{Ip}^k}{m_I^k},$$

(81)

$$v_{ip}^{k+1/2} = v_{ip}^{k-1/2} + \Delta t^k \sum_{I=1}^{n_g} \frac{f_{iI}^k N_{Ip}^k}{m_I^k},$$

(82)

and update the phase field d_p by

$$d_p^{k+1} = d_p^k + \sum_{I=1}^{n_g} N_{Ip} \Delta d_I^k.$$

(83)

(5) Impose the monotonically increasing condition and the value constraint of the phase field by

$$d_p^{k+1} = \begin{cases} d_p^{k+1} & d_p^{k+1} > d_p^k \\ d_p^k & d_p^{k+1} \leqslant d_p^k, \end{cases}$$

(84)

$$d_p^{k+1} = \begin{cases} 1 & d_p^{k+1} > 1 \\ d_p^{k+1} & d_p^{k+1} \leqslant 1, \end{cases}$$

(85)

and update the gradient of the phase field by

$$d_{p,i}^{k+1} = \sum_{I=1}^{n_g} N_{Ip,i} \sum_{q=1}^{n_p} N_{Iq} d_q^{k+1}.$$

(86)

(6) Reconstruct the grid momentum from updated MPM particles by

$$p_{iI}^{k+1/2} = \sum_{p=1}^{n_P} m_p v_{ip}^{k+1/2} N_{Ip}^k,$$

(87)

and impose the essential boundary condition. Calculate the updated grid node velocity by

$$v_{iI}^{k+1/2} = \frac{p_{iI}^{k+1/2}}{m_I^n}.$$

(88)

(7) Calculate the incremental strain and incremental vorticity of particles by

$$\Delta \varepsilon_{ijp}^{k+1/2} = \Delta t^{k+1/2} \sum_{I=1}^{n_g} \frac{1}{2} \left(N_{Ip,j}^k v_{iI}^{k+1/2} + N_{Ip,i}^k v_{jI}^{k+1/2} \right),$$

(89)

$$\Delta \Omega_{ijp}^{k+1/2} = \Delta t^{k+1/2} \sum_{I=1}^{n_g} \frac{1}{2} \left(N_{Ip,j}^k v_{iI}^{k+1/2} - N_{Ip,i}^k v_{jI}^{k+1/2} \right),$$

(90)

and then update the stress of particles by a constitutive model, and density by

$$\rho_p^{k+1} = \frac{\rho_p^n}{(1 + \Delta \varepsilon_{iip}^{k+1/2})}.$$

(91)
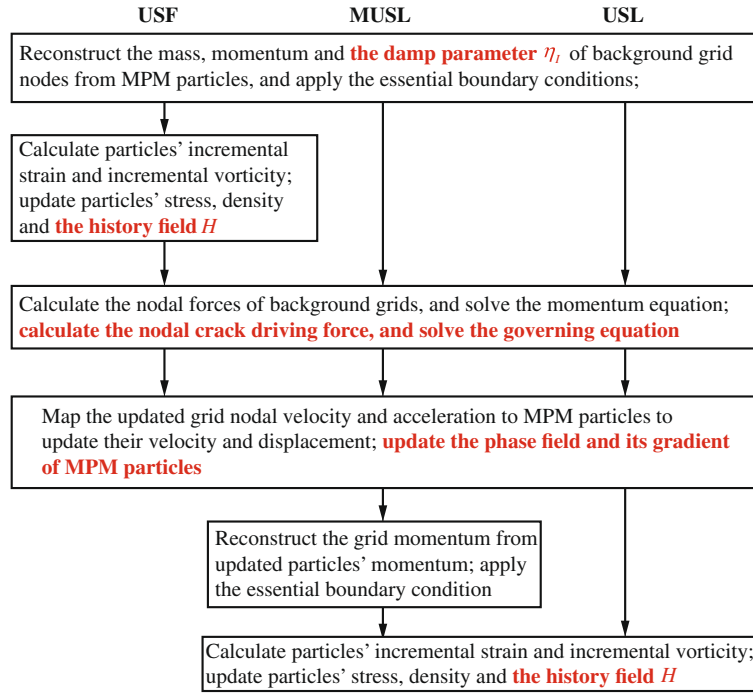
The flow chart of the ex-PFMPM is summarized in Figure 4.

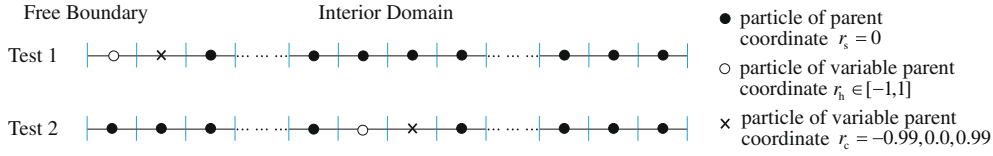**FIGURE 4** Flow chart of the explicit phase field material point method (ex-PFMPM).

FIGURE 5 Verification tests for 1D formula.

4 | NUMERICAL EXAMPLES

4.1 | Verification of the proposed critical time step formulae

As shown in Figure 5, an 1D computational domain is divided into a set of cells with one particle in each cell. Particles represented by the solid dot are set at the cell centers with particle coordinate $r_s = 0.0$. The parent coordinate of the particle represented by the hollow dot varies from -1 to 1, which represents different particle positions. And the parent coordinate of the particle represented by the cross mark is chosen from three values, namely, $-0.99, 0.00$, and 0.99, which is designed to demonstrate the effect of neighboring cell interaction on the critical time step together with the particle of hollow dot. The two particles with hollow dot and cross mark are set at the different locations in the computational domain, namely, the free boundary (Test 1) and the interior domain (Test 2) to verify the critical time formula in different conditions.

We assume the crack energy release rate $G_c = 1 \, \text{J/m}^2$, the section area $A = 1 \, \text{m}^2$, the viscous dissipation parameter $\eta = 1$, the cell side length of the background grids $l = 0.01 \, \text{m}$ and the regularization parameter $l_c = 2l = 0.02 \, \text{m}$. The exact critical time step $\Delta t_{cr}^{100-cell}$ will be calculated directly by solving the system eigenvalue problem.

In the existing literature, the critical time step is usually determined by Wang[20]

$$\Delta t_{est} = \frac{L_{min}^2}{2\alpha}, \quad \alpha = G_c l_c / \eta, \tag{92}$$

where L_{min} is the minimum characteristic scale of the cell, which equals to l in this example. In order to compare the critical time step obtained by our formulae with that used in the existing literature, the ratio R of the critical time step

Δt_{cr}, calculated by solving the system eigenvalue problem of the 100-cell system and the 2-cell formulae Equations (57) and (63), to Δt_{est} is investigated, namely,

$$R = \Delta t_{\text{cr}}/\Delta t_{\text{est}}. \tag{93}$$

The critical time step of the explicit phase field method without considering the effect of the history field H (i.e., $H = 0$) is examined first. Figures 6 and 7 plot the ratio R versus the parent coordinate r_h of the particle with hollow dot obtained by directly solving the system eigenvalue problem of the 100-cell system and the 2-cell formulae based on the moving mesh MPM and standard MPM for Test 1 and Test 2. As shown in Figures 6 and 7, the critical time step based on the moving mesh MPM underestimates the critical time step regardless of the parent coordinate of particle with hollow circle, because it ignores the effect of the Eulerian parts of the standard MPM. It is worth to be mentioned that the minimum value of the ratio of the standard MPM is higher than that of the moving mesh MPM. Furthermore, when the parent coordinate of particle with hollow circle $r_h \rightarrow 1.0$ in Figure 6A, $r_h \rightarrow 1.0$ in Figure 6B, and $r_h \rightarrow -1.0$ or 1.0 in Figure 6C, the critical time step will severely decrease to 0. As discussed in Ni and Zhang,[42] the critical time step in MPM will considerably decrease because of the small nodal mass when particles are near the cell boundary. Similarly, when particles distribute near the cell boundary in ex-PFMPM, a small nodal viscous dissipation value will be obtained at the opposite cell boundary, which causes a severely small critical time step. However, on the contrary, the ratio of the standard MPM always keep $R > 1$ no matter what the parent coordinate of particle with hollow circle is. The same situation arises when the parent coordinate of particle with hollow circle $r_h \rightarrow -1.0$ in Figure 7B. As shown in Figures 6B and 7B, $\Delta t_{\text{cr}}^{2-\text{cell}} = \Delta t_{\text{cr}}^{100-\text{cell}}$ when the parent coordinate of the particle with hollow circle $r_h = 0.0$. It means that the 2-cell formula can give a precise critical time step when all the particles are at the center of the cell, and thus our formula based on the Gerschgorin's theorem can also
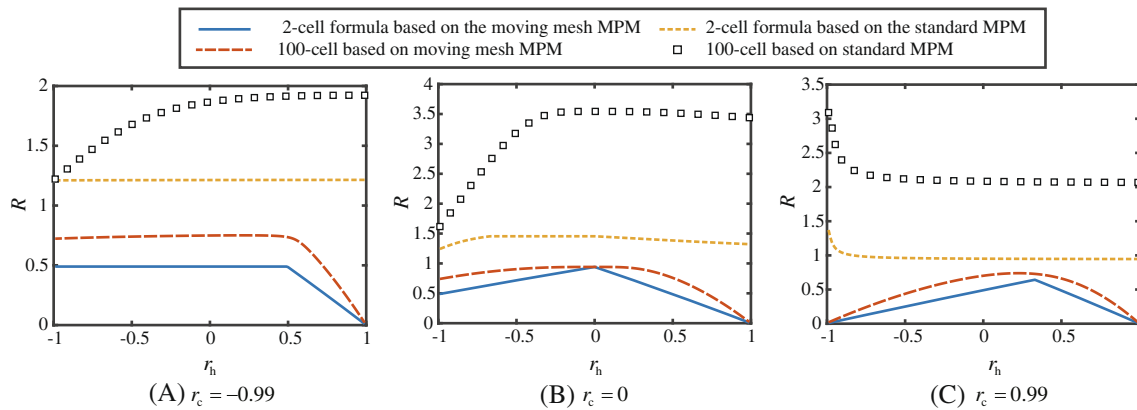

FIGURE 6 The ratio R versus the parent coordinate r_h for Test 1.
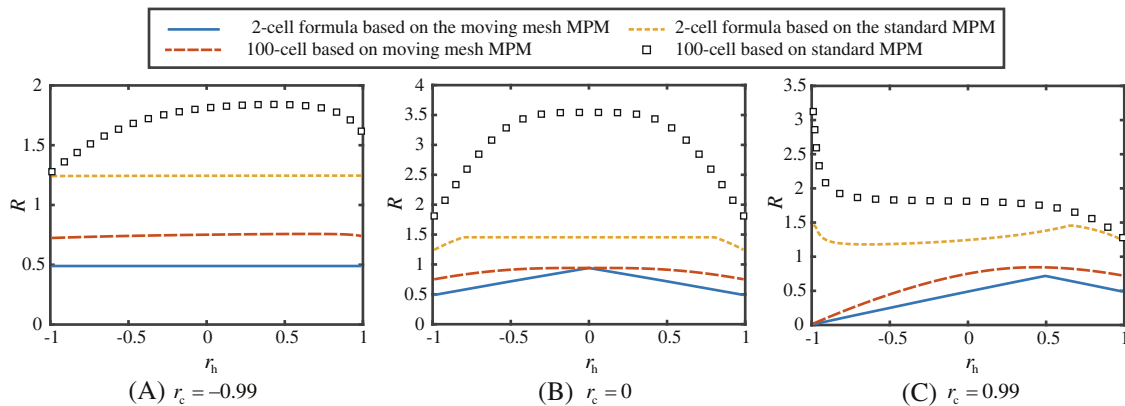

FIGURE 7 The ratio R versus the parent coordinate r_h for Test 2.

provide a satisfactory estimation for the critical time step in the PF-FEM with single-point Gaussian quadrature and the lumped mass matrix. The above analysis also indicates that the ex-PFMPM is more stable than an explicit phase field FEM.

By comparing the results given by directly solving the system eigenvalue problem of the 100-cell system and the 2-cell formula of the standard MPM shown in Figures 6 and 7, we find that the 2-cell formula underestimates the critical time step due to the Gerschgorin's theorem, thus guarantees the stability of the simulation process. Besides, the underestimation of the critical time step remains at an acceptable level, that is, $\Delta t_{\mathrm{cr}}^{2-\mathrm{cell}} > 0.4 \times \Delta t_{\mathrm{cr}}^{100-\mathrm{cell}}$ for any particle distribution.

When applying the 2-cell formulae Equations (57) and (63) for practical use, the effect of the strain energy of particles needs to be considered. We assume the history field $H = 10G_{\mathrm{c}}/l_{\mathrm{c}}$ for all particles in Equations (57) and (63), and the ratio R versus the parent coordinate r_{h} of the particle with hollow dot obtained by directly solving the system eigenvalue problem of the 100-cell system and the 2-cell formulae Equations (57) and (63) in Test 1 and Test 2 are depicted in Figures 8 and 9, respectively. Compared to the ratio R shown in Figures 6 and 7, the tendency of the ratio R versus the parent coordinate r_{h} of the particle with hollow dot is similar, but the critical time step significantly decreases as the 2-cell formula Equations (57) and (63) predicts. This illustrated the effect of the strain energy on the critical time step, and the widely used estimated formula Equation (92) will severely overestimate the critical time step, which will lead to instablility during the simulation. And the critical time step given by the 2-cell formula is closer to the critical time step given by the system eigenvalue in the high stain energy level compared to that in Figures 6 and 7, which indicates that the 2-cell formula can give a satisfactory prediction in the numerical application.

To validate the extension of the 1D 2-cell formula of ex-PFMPM to 2D and 3D, a 2D test as shown in Figure 10 is studied. There are 20 cells in each direction and only one particle in each cell. The parent coordinate r_{h} and s_{h} of the hollow dot varies in $[-1, 1]$ which represents different particle position in the cell, and all the particles represented by the solid dot are at cell centers whose parent coordinate $r_0 = 0, s_0 = 0$.
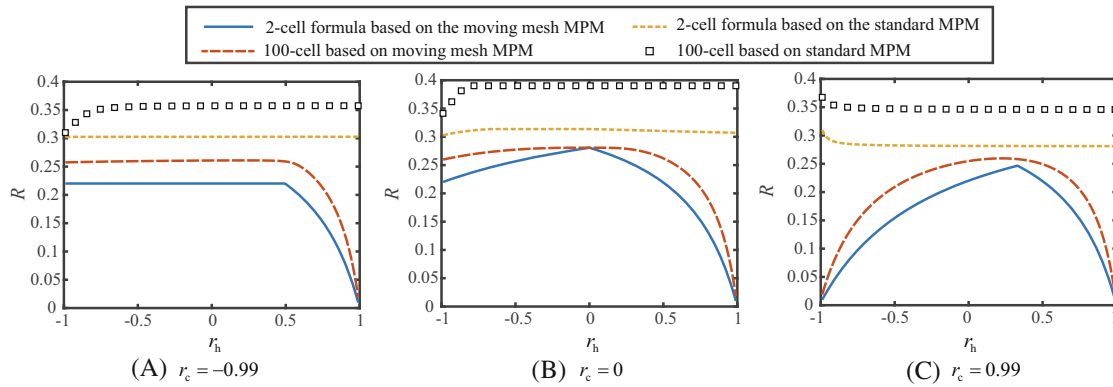

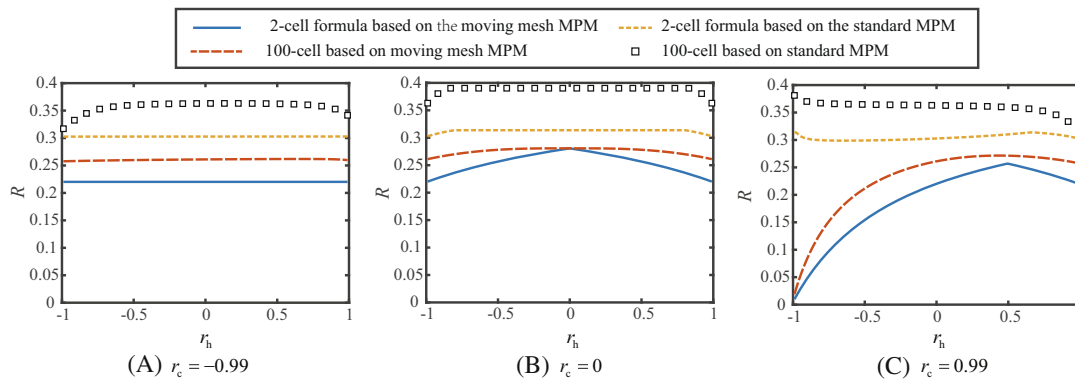**FIGURE 8** The ratio R versus the parent coordinate r_{h} for Test 1 with history field $H = 10G_{\mathrm{c}}/l_{\mathrm{c}}$.

FIGURE 9 The ratio R versus the parent coordinate r_{h} for Test 2 with history field $H = 10G_{\mathrm{c}}/l_{\mathrm{c}}$.
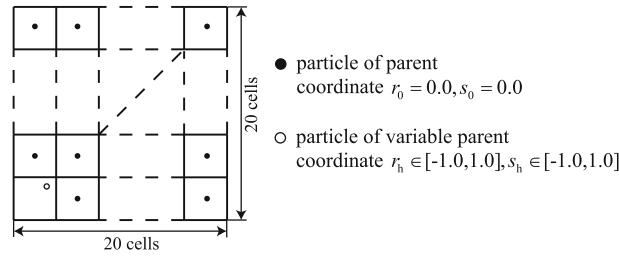
FIGURE 10 Diagram of 2D test for the extended 1D 2-cell formula.

(A) Extended 1D 2-cell formula (B) 400-cell System Eigenvalue (C) Ratios $R_1 = \Delta t_{cr}^{2\text{-cell}} / \Delta t_{cr}^{400\text{-cell}}$

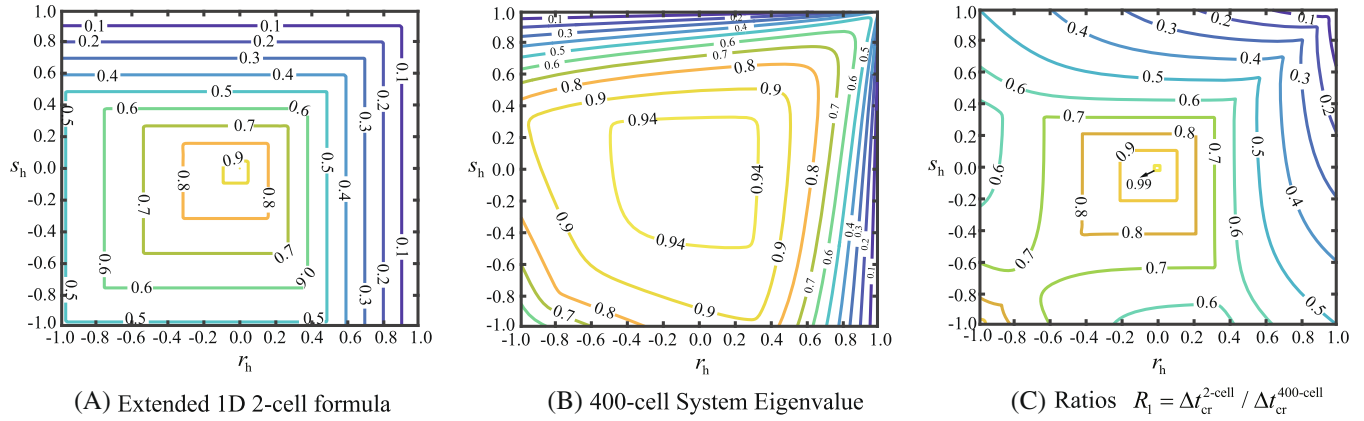**FIGURE 11** The critical time step versus the parent coordinate based on moving mesh material point method (MPM).
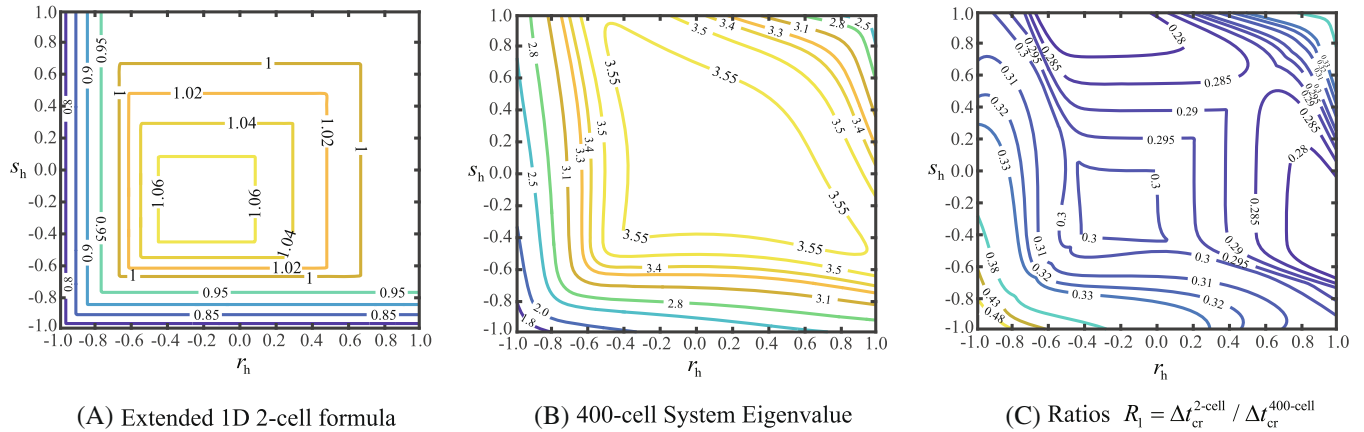

(A) Extended 1D 2-cell formula (B) 400-cell System Eigenvalue (C) Ratios $R_1 = \Delta t_{cr}^{2\text{-cell}} / \Delta t_{cr}^{400\text{-cell}}$

FIGURE 12 The critical time step versus the parent coordinate considering Eulerian parts.

To investigate the effect of the strain energy on the critical time step, we first assume the history field $H = 0$. Figures 11A and 12A show the $R^{2\text{-cell}}$ ratio contour defined in Equation (93) of the critical time step versus the parent coordinates r_h and s_h of the hollow dot with extended 1D 2-cell formula Equation (64) of the ex-PFMPM based on the moving mesh MPM and standard MPM. Figures 11B and 12B show the $R^{400\text{-cell}}$ ratio contour given by solving the 400-cell system eigenvalue problem of the ex-PFMPM based on the moving mesh MPM and standard MPM. And Figures 11C and 12C show the ration $R_1 = R^{2\text{-cell}}/R^{400\text{-cell}}$ of the critical time step given by the extended 1D 2-cell formula to the critical time step given by solving the 400-cell system eigenvalue problem of the ex-PFMPM based on the moving mesh MPM and standard MPM.

As Figure 11A shows, in the moving mesh MPM, the isohypse of the ratio keeps vertical or horizontal because the extension of the 1D 2-cell formula is based on the mesh orthogonality, while the ratio isohypse in Figure 11B is oblique

and symmetry to the diagonal because the particles are symmetric to the diagonal. The critical time step is much larger when the hollow dot is near the left-bottom corner than other three corners. It is because that the decoupled volume V_{xI}^n or V_{yI}^n of the grid node in left-bottom corner will decrease sharply to 0 when the particle with hollow dot is near the three other corners, while the decoupled volume V_{xI}^n or V_{yI}^n will increase to V_p^n when the particle with hollow dot is near the left-bottom and the decoupled volume V_{xI}^n or V_{yI}^n of the other grid nodes will not turn to infinitely small. However, as shown in Figure 12A,B, in the ex-PFMPM based on the standard MPM, the particle position has comparatively small impact on the critical time step, and the stability of the ex-PFMPM based on the standard MPM is much better than the ex-PFMPM based on the moving mesh MPM. As Figure 11C shows the extended 1D 2-cell formula can give a fairly accurate prediction of the critical time step in most part of the cell. No matter where the hollow particle is, the ratios R_1 is always smaller than 1, which means that the critical time step given by the extended 1D 2-cell formula can guarantee the simulation stability. However, near the right-top corner, the ratios R_1 of the critical time step will sharply decrease along the diagonal direction which is observed in the critical analysis in the standard MPM.[42] However, as shown in Figure 12C, in the ex-PFMPM based on the standard MPM, the value of R_1 is rather small, because the 2-cell formula of the ex-PFMPM based on the standard MPM highly underestimate the critical time step.

Next we assume the history field $H = 10G_c/l_c$ to investigate the effect of the strain energy on the critical time step, and the results are shown in Figures 13 and 14. In the ex-PFMPM based on the moving mesh MPM, the distribution and direction of the isohypse in Figure 13A,B are similar to those in Figure 11A,B, respectively, except for the values of the isohypse which are all under 0.3 and much smaller than those without the effect of the strain energy. And comparing Figures 13C with 14C, the value of the isohypse in Figure 14C is much larger, which means the extension of the 2-cell
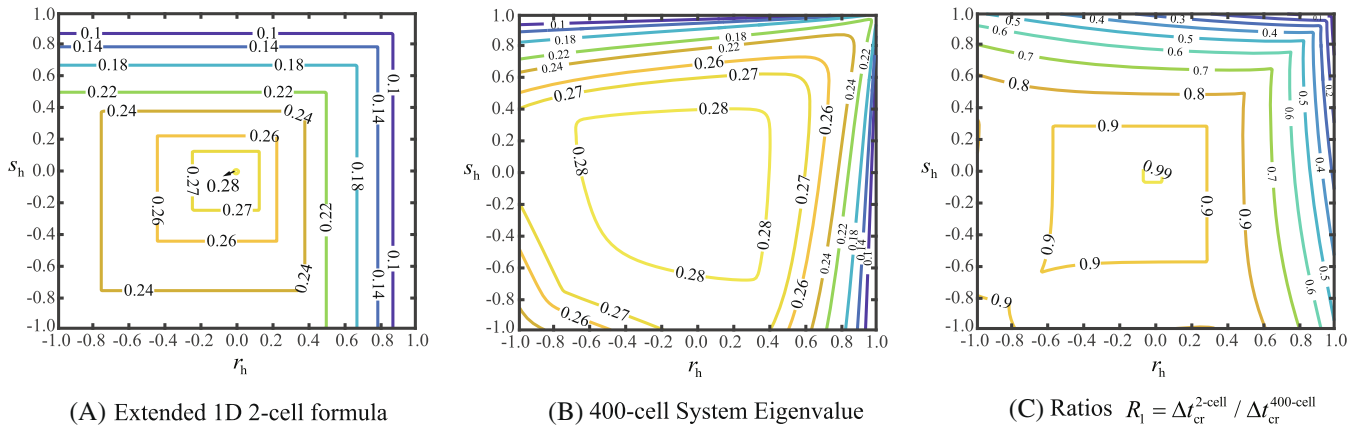

(A) Extended 1D 2-cell formula   (B) 400-cell System Eigenvalue   (C) Ratios $R_1 = \Delta t_{cr}^{2\text{-cell}} / \Delta t_{cr}^{400\text{-cell}}$

FIGURE 13   The critical time step versus the parent coordinate based on moving mesh material point method (MPM) with history field $H = 10G_c/l_c$.

(A) Extended 1D 2-cell formula   (B) 400-cell System Eigenvalue   (C) Ratios $R_1 = \Delta t_{cr}^{2\text{-cell}} / \Delta t_{cr}^{400\text{-cell}}$
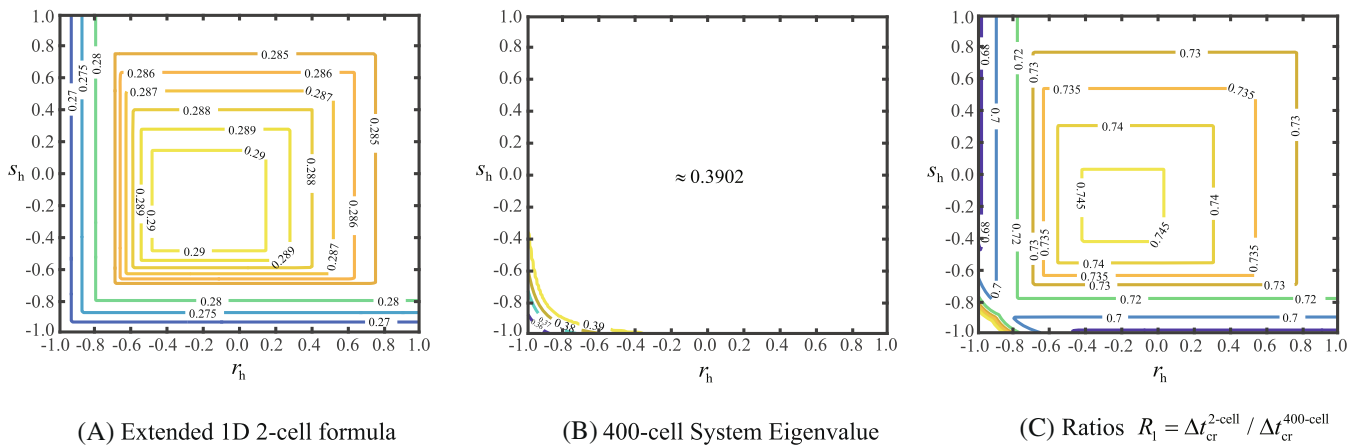
FIGURE 14   The critical time step versus the parent coordinate considering Eulerian parts with history field $H = 10G_c/l_c$.

formula can give a more precise estimation for critical time step in practical use. In the the ex-PFMPM based on the standard MPM, the distribution and direction of the isohypse in Figure 13A is similar to those in Figure 12A, but the ratio given by solving the 400-cell system eigenvalue problem almost remain unchanged $R_{400-\text{cell}} \approx 0.39$ as shown in Figure 14B.

4.2 | 1D string with pre-existing crack

To verify the theoretical analysis in Section 3.3, a practical numerical example in one-dimensional condition is considered in this section. As shown in Figure 15, a concentrated force F_1 is applied at the left end of a 1D string with a pre-existing crack in the middle. We set the Young's modulus $E = 10$ MPa, material density $\rho = 1000$ kg/m^3, section area $A = 1$ m^2, total length $L = 1$ m and the crack energy release rate $G_c = 1$ J/m^2. And, the computational domain is discretized into 100 uniform cells of length $l = 0.01$ m with 1 particle in each cell. The viscous dissipation parameter $\eta = 1$, and the regularization parameter $l_c = 2l = 0.02$ m. All the numerical examples in these Sections 4.3–4.5 are simulated by the standard MPM.

Three tests are carried out. In Test 1, a pure phase field evolution problem is studied, in which the concentrated force $F_1 = 0$. The two constraint conditions Equations (84) and (85) of the phase field are not imposed, because they will enhance the stability and are difficult to be considered in the theoretical analysis. The time step size used in each step is determined by

$$\Delta t = \text{CFL} \times \Delta t_{\text{cr}}, \tag{94}$$

where Δt_{cr} is obtained by directly solving the system eigenvalue problem.

The error $e = |\sum_{p=1}^{n_p} d(x_p)|/n_p$ obtained with different parent coordinate r_h are plotted in Figure 16. As Figure 16 shows, the phase field update is stable when the CFL number equals 0.99 and unstable when CFL number equals 1.01 for all three different parent coordinate r_h of the hollow dot, which means that the critical time step given by the system eigenvalue is the exact value of the critical time step. And it verifies our theoretical analysis in Section 3.3.
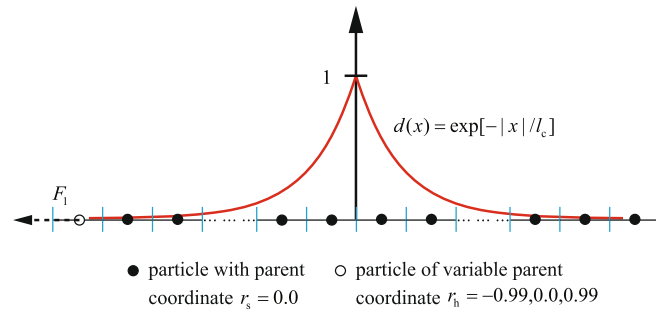

FIGURE 15 One-dimension string with pre-existing crack for explicit phase field material point method (ex-PFMPM) test.
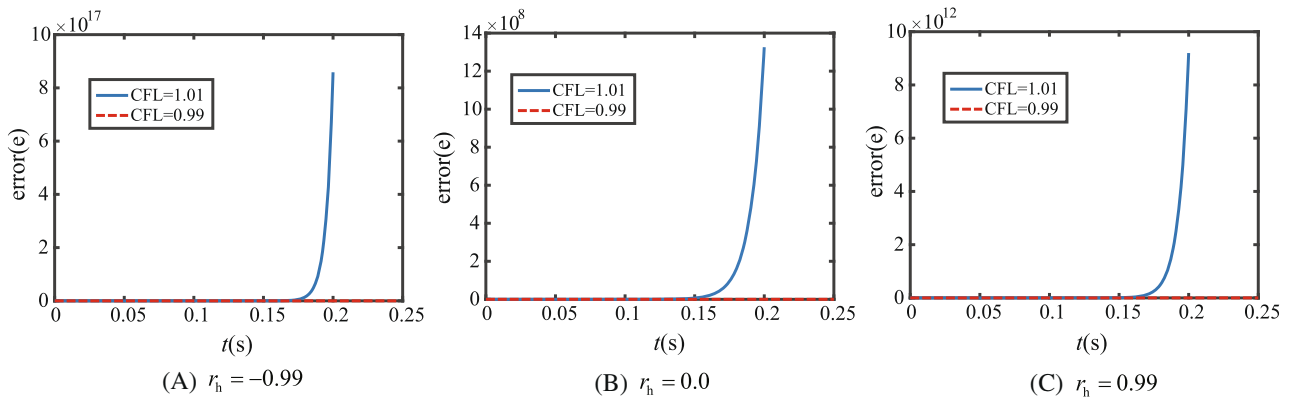

(A) $r_h = -0.99$

(B) $r_h = 0.0$

(C) $r_h = 0.99$

FIGURE 16 The calculation error of different parent coordinate ξ_h.

In Test 2, the effect of the strain energy is studied. The concentrated force F_1 applied at the left end is set to $F_1 = 0.1\,\text{N}$. And the two constraint conditions Equations (84) and (85) of the phase field are considered. The displacements of the 1D string at time $t = 0.1\,\text{s}$ obtained with different time step sizes are shown in Figure 17A. The reference solution is the simulation result obtained with 10,000 particles. As shown in Figure 17A, all simulations with time step size determined by different estimation methods give stable simulation results. However, the simulation with 2-cell formula is the most efficient as shown in Table 1. Compared to the critical time step determined by Equation (92), the 2-cell formula can give a bigger time step which leads to less simulation steps. And compared to the critical time step determined by the system eigenvalue, the 2-cell formula does not need to calculate the system eigenvalue which leads to less simulation cost in each step, and results in higher simulation efficiency. And in the simulation with huge degree of freedom, the extra simulation and storage cost of solving the system eigenvalue problem is prohibitive.

In Test 3, we set the concentrated force $F_1 = 20\,\text{N}$ and the crack energy release rate $G_c = 0.2\,\text{J/m}^2$. With this parameter setting, the strain energy will seriously influence the critical time step of ex-PFMPM. And the two constraint conditions Equations (84) and (85) of the phase field are considered. The displacement of the 1D string at time $t = 0.1\,\text{s}$ obtained with different time step sizes are plotted in Figure 17B. As shown in Figure 17B, the simulation with time step size based on the system eigenvalue and the 2-cell formula can give a stable simulation result, but the estimated time step given by Equation (92) leads to an unstable simulation because of the ignoring of the strain energy in Equation (92). As shown in Table 2, the simulation with the 2-cell formula is more efficient than that with the system eigenvalue. And the simulation time difference is much bigger than that in Test 2, because the critical time step determined by the 2-cell formula is closer
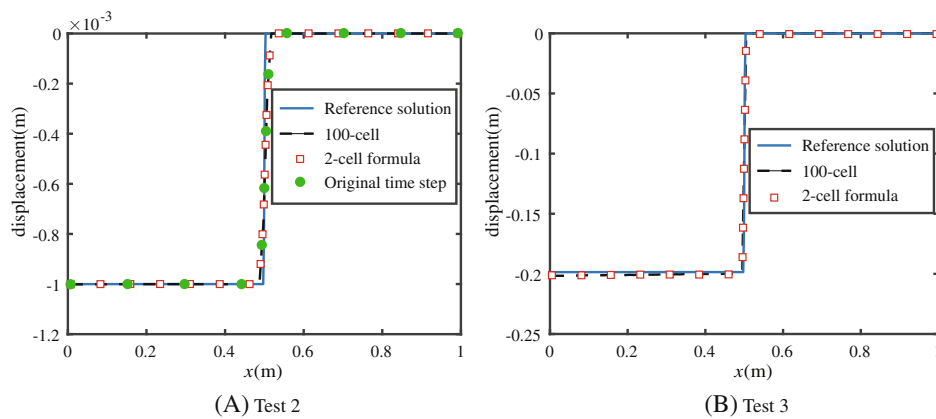

FIGURE 17 The displacement of the 1D string at time $t = 0.1\,\text{s}$.

TABLE 1 Simulation time and steps of different method in Test 2.

Critical time step formula	Total simulation time for physical simulation time 0.1 s	Total steps for physical simulation time 0.1 s
Original	1.013 s	4002
2-cell formula	0.619 s	2668
100-cell	2.761 s	1202

TABLE 2 Simulation time and steps of different method in Test 3.

Critical time step formula	Total simulation time for physical simulation time 0.1 s	Total steps for physical simulation time 0.1 s
Original	Unstable	Unstable
2-cell formula	0.738 s	3179
100-cell	5.007 s	2075

to the critical time step determined by the system eigenvalue in the high stain energy level. This will lead to the less simulation step difference.

In summary, the time step determined by the 2-cell formula is an efficient and relatively accurate estimation of the precise critical time step, which is worth employed in numerical applications. In the next three section, the 2-cell formula is used to determine the time step.

4.3 | Dynamic crack branching

In this section, a dynamic crack branching process of a central crack in a plate under transient tensile loading is studied. As shown in Figure 18, the specimen's length $L_1 = 100$ mm, width $L_2 = 40$ mm and thickness $t = 1$ mm. The length of the initial crack equals to 50 mm. The tensile stress of 1.0 MPa is applied continuously on the top and bottom surfaces of the plate. The material density is 2450 kg/m^3, Young's modulus and Poisson's ratios are 32.0 GPa and 0.2, respectively, and the energy release rate $G_c = 3.0$ J/m^2. The specimen is discretized by a set of particles with a spacing of $\Delta = 0.25$ mm, and the side length of the background grid cell for MPM is chosen as $l = 0.5$ mm. The critical length $l_c = 2l = 1$ mm, and the viscous dissipation parameter $\eta = 0.01$. The total number of particles and the backgroud cells are 256,000 and 172,800, respectively. During the simulation, the minimum time step size $\Delta t = 1.20 \times 10^{-8}$ s, and the total number of time steps $N_{step} = 8076$. This problem has been experimentally investigated by Sharon et al.[43] and Fliss et al.[44] and numerically studied by Belytschko et al.[45] by XFEM and Borden et al.[10] by phase field method. These experimental and numerical studies have shown that the crack will branch in the process of rapid propagation.

To test the influence of history field in the ex-PFMPM, the dynamic crack branching problem is simulated with and without considering the history field H, respectively. The evolution of the phase field without considering the history field is presented in Figure 19. The occurrence of a branched crack is observed at approximately $t = 35$ μs and the crack tip reaches at the material boundary at approximately $t = 80$ μs, which agree well with the reported simulation results.[10,29]
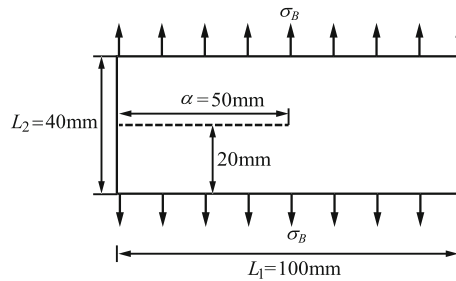

FIGURE 18 A plate with a central crack under transient tensile loading.

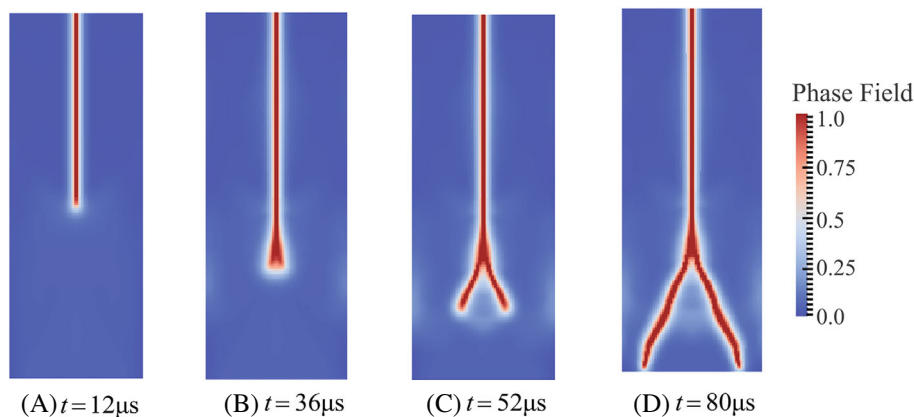(A) $t = 12\mu s$ (B) $t = 36\mu s$ (C) $t = 52\mu s$ (D) $t = 80\mu s$

FIGURE 19 Evolution of the phase field through time in original configuration.

Furthermore, the crack branching path and the distance between two crack tips near the material boundary is similar to the reported results.[10,29] Besides the evolution of the phase field considering the history field is presented in Figure 20. The occurrence of the crack branching and the crack path is similar to the results shown in Figure 19, but the crack area is slightly wider. This is because of the overestimation of the crack driving force with the use of history field, and a more detailed comparison will be raised in the next section. The total strain energy and fracture energy during the simulation process are shown in Figure 21A,B. The fracture energy is calculated by the particle integration of the following equation

$$E_\mathrm{f} = G_\mathrm{c} \int_\Omega \left(\frac{1}{2l_\mathrm{c}} d^2 + \frac{l_\mathrm{c}}{2} d_{,i} d_{,i} \right) \mathrm{d}\Omega. \tag{95}$$

The total elastic strain energies plotted in Figure 21A demonstrate good agreement to Bordon's Result, and the result of the ex-PFMPM is more precise than the PFMPM with implicit time integration[29] after $t > 30~\mu s$, and the result between the ex-PFMPM with and without considering the history field H is minor. The total fracture energy results shown in Figure 21B are in perfect agreement with the results reported by Borden et al.[10] Minor differences are observed in the PFMPM with implicit time integration especially for time $t > 40~\mu s$, but the results of the ex-PFMPM shows perfect agreement.

4.4 | Plate with a pre-existing crack under velocity boundary conditions

In this section, the crack growth is simulated. As shown in Figure 22A, an isotropic plate with a pre-existing crack in the center is subjected to a velocity boundary condition on its horizontal edges. The initial length of the crack $2a_0 = 10~\mathrm{mm}$,
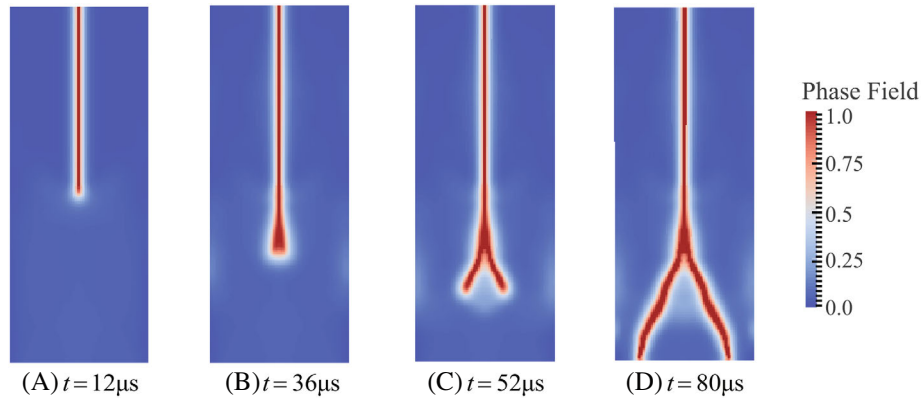

(A) $t = 12\mu s$ (B) $t = 36\mu s$ (C) $t = 52\mu s$ (D) $t = 80\mu s$

FIGURE 20 Evolution of the phase field through time in original configuration with history field.

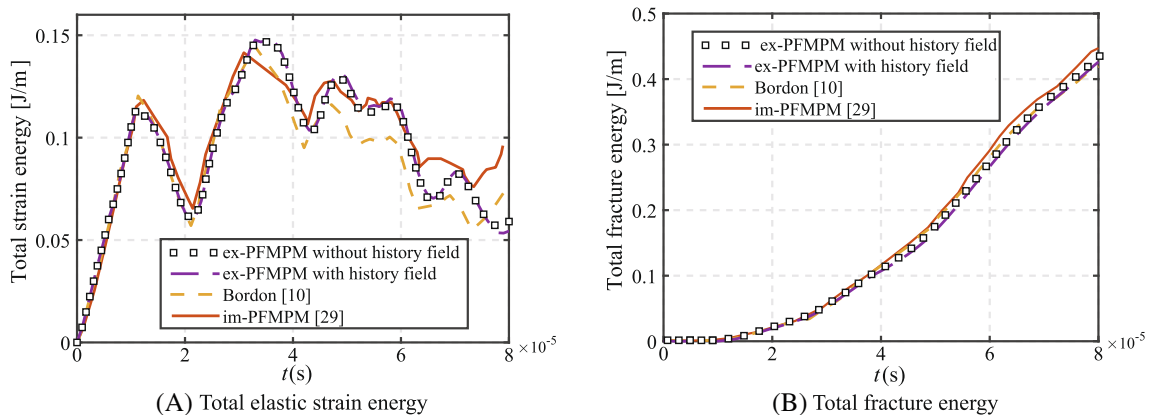(A) Total elastic strain energy   (B) Total fracture energy

FIGURE 21 Plate under impact loading: (A) Total elastic strain energy; (B) Total fracture energy.
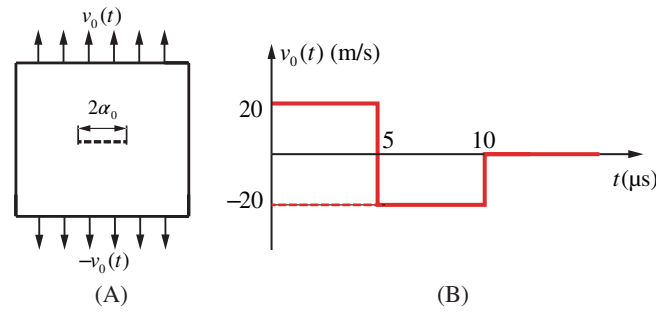
FIGURE 22 Plate with a pre-existing crack under velocity boundary conditions.

(A) $t = 6\mu s$ (B) $t = 8\mu s$ (C) $t = 10\mu s$

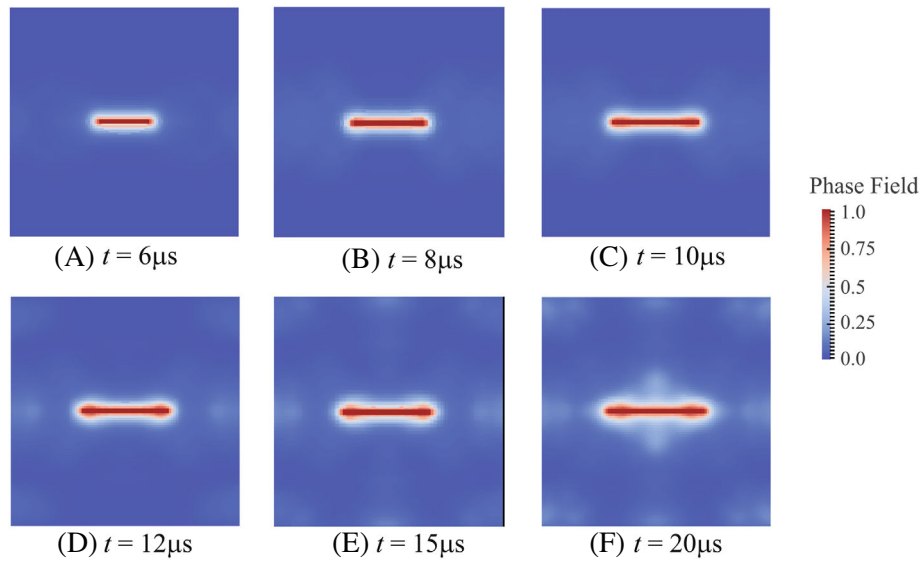(D) $t = 12\mu s$ (E) $t = 15\mu s$ (F) $t = 20\mu s$

FIGURE 23 Evolution of the phase field in the original configuration with history field.

the material density, Young's modulus and Poisson's ratios are 8000 kg/m³, 192 GPa, and 1/3, respectively. The length and thickness of the square plate are 50 and 0.1 mm, respectively. The specimen is discretized by a set of particles with a spacing of $\Delta = 0.1$ mm, and the side length of the background grid cell for MPM is chosen as $l = 0.2$ mm. The critical length $l_c = 2l = 0.4$ mm, and the viscous dissipation parameter $\eta = 10$. The total number of particles and the backgroud cells are 250,000 and 90,000, respectively. During the simulation, the minimum time step size $\Delta t = 1.47 \times 10^{-9}$ s, and the total number of time steps $N_{step} = 13,044$. The critical energy release rate $G_c = 8.8 \times 10^4$ J/m², and the velocity boundary conditions are applied as shown in Figure 22B. The degradation function in this problem is taken as

$$g_d(d) = [1 + (2 - s)d](1 - d)^2, \tag{96}$$

where $s \in [0, 2]$ is a positive constant. Compared to the quadratic degrade function Equation (12), the degrade function (96) can make the material keep elastic before the phase field reaches a higher value because $s \to 0$ gives $(\partial g_d(d)/\partial d)_{d=0} \to 0$. When $s \to 2$, the degradation function degrades to the quadratic function. This degradation function is employed to reduce the fake phase field update in the nonfracture area.

This numerical example is designed to show the difference of the solution of ex-PFMPM with and without considering the history field H. The plate is loaded when $0 \ \mu s < t < 5 \ \mu s$ and unloaded when $5 \ \mu s < t < 10 \ \mu s$, as shown in Figure 22B. When considering the history field H, the crack driving force will not decrease during the unloading process, which may lead to fake phase field increase as aforementioned. To verify this hypothesis, the evolution of the phase field obtained with and without considering the history field are presented in Figures 23 and 24, respectively. This problem was numerically

studied by Silling and Askari[46] with Peridynamics (PD), and the crack growth distance and the fracture energy obtained by the ex-PFMPM and PD are shown in Figure 25A,B.

As shown in Figures 23 and 24, both solutions can simulate the crack growth process which starts at about $t = 6$ μs and stops at about $t = 10$ μs. And the crack growth distance also shows good agreement with the PD result.[46] However, comparing the results of two solutions of ex-PFMPM, the crack area is obviously wider in the solution considering the history field at all time instants. And the phase field value in the nonfracture area obtained with considering the history field is obviously larger than that without considering the history field, which means the fake phase field update happens. Furthermore, the fake phase field update also leads to a fake crack growth at about $t = 15$ μs, which indicates that in some extreme conditions considering the history field may cause poor prediction of the crack growth path. A more distinct evidence of the fake phase field update can be seen in Figure 25B. The total fracture energy obtained with considering the history field is obviously larger than that without considering the history field and PD. In the theory of fracture dynamics, the fracture energy will not change after the crack growth process stops at $t = 10$ μs as shown by the PD results in Figure 25B. However, the fracture energy of the two solutions of ex-PFMPM keeps increasing after the the crack growth process stops, because the phase field is still updating, which is a fundamental characteristic of the phase field method. And the fracture energy obtained by the ex-PFMPM with considering the history field have much larger deviation to
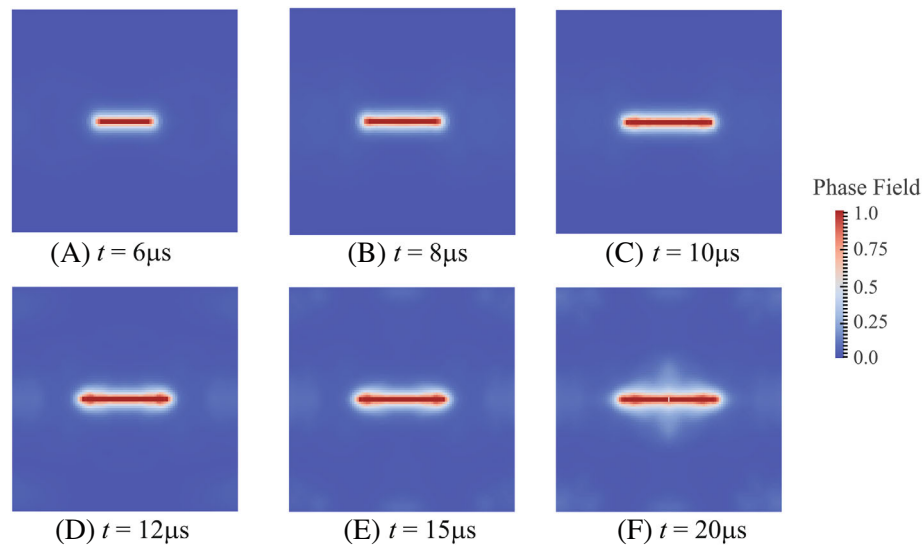

(A) $t = 6\mu$s (B) $t = 8\mu$s (C) $t = 10\mu$s (D) $t = 12\mu$s (E) $t = 15\mu$s (F) $t = 20\mu$s

FIGURE 24 Evolution of the phase field in the original configuration without history field.

(A) Crack growth distance of different solutions (B) Total fracture energy of different solutions
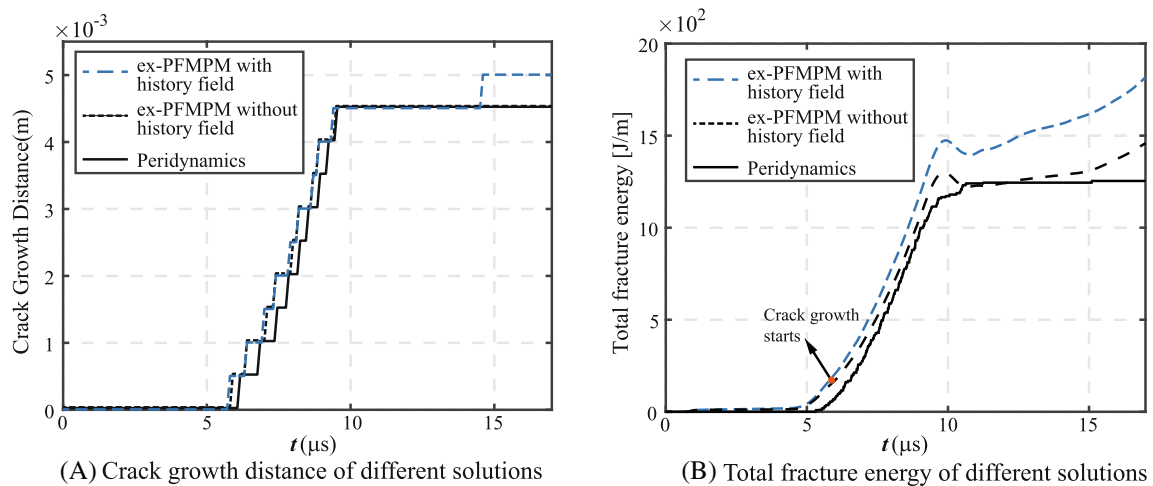
FIGURE 25 Crack growth distance and total fracture energy of different solution.

the PD, compared to the results without considering the history field, which is because of the fake phase field update. Besides, the fracture energy obtained by the ex-PFMPM has a little decrease at $t = 10\ \mu$s, which is counterintuitive. It is because of that only the monotonic increasing condition of the phase field d is guaranteed, but the monotonic increasing condition of its gradient in Equation (95) can not be guaranteed, so the monotonic increasing of the fracture energy can not be guaranteed.

4.5 | Three-point bending

As shown in Figure 26, a three-point bending specimen with an edge crack is subjected to an eccentric impact. The specimen's length $L_1 = 400$ mm, width $L_2 = 100$ mm, thickness $t = 10$ mm. The length of the initial crack equals to 50 mm. The material density is 1190 kg/m^3, Young's modulus and Poisson's ratios are 2.94 GPa and 0.3, respectively, and the energy release rate $G_c = 4.9 \times 10^2$ J/m^2. The impactor is a cylindrical body, which has a mass of $m = 5.05$ kg and an initial velocity of $v_0 = 5$ m/s. The material of the stiff impactor is modeled with $E_i = 200$ GPa and $v_i = 0.25$. The impact loading eccentricity is defined as $e = 2l/L_1$. Nishioka and his co-workers studied this eccentric impact fracture experiments with different loading eccentricity. This problem has been simulated by Guo and Nairn using CRAMP,[47] and by Liang et al. using XMPM[48] with different crack incremental length.

To simulate this problem by ex-PFMPM without considering the history field, the specimen is discretized into a set of particles with a spacing of $\Delta = 1$ mm, and the side length of the background grid cell for MPM is chosen as $l = 2$ mm. The critical length $l_c = 2l = 4$ mm, and the viscous dissipation parameter $\eta = 0.1$. The total number of particles of the specimen and the backgroud cells are 400,000 and 154,350, respectively. During the simulation, the minimum time step size $\Delta t = 7.59 \times 10^{-8}$ s, and the total number of time steps $N_{step} = 4354$. The impact between the specimen and the impactor is modelled by the contact algorithm proposed by Ma et al.[49]

As shown in Figure 27A, the central impact with $e = 0.0$ is modeled first. Due to the symmetry of the problem, the crack will grow along its initial crack plane as the stretch wave arrives the crack tips. Figure 28 gives the crack length versus time obtained by the CRAMP, experiment, XMPM and ex-PFMPM. The results show that the ex-PFMPM and
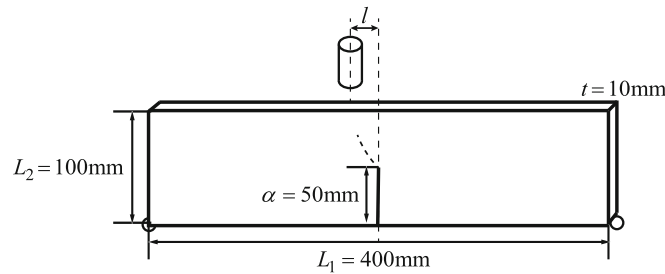

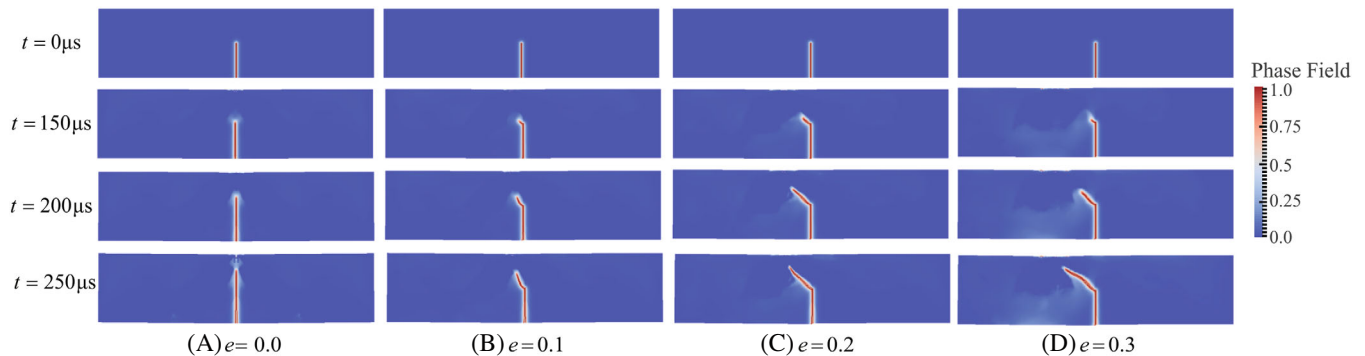**FIGURE 26** A three-point bending specimen subjected to the eccentric impact.

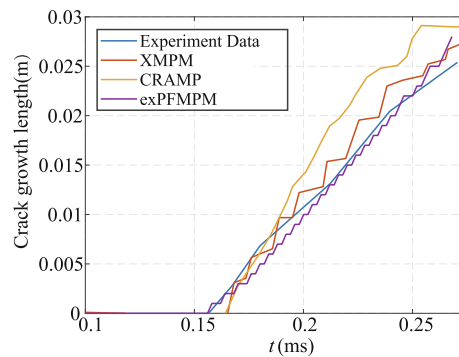**FIGURE 27** The evolution of the crack with different eccentricity.

FIGURE 28 Crack growth length of different simulation method with $e = 0.0$.
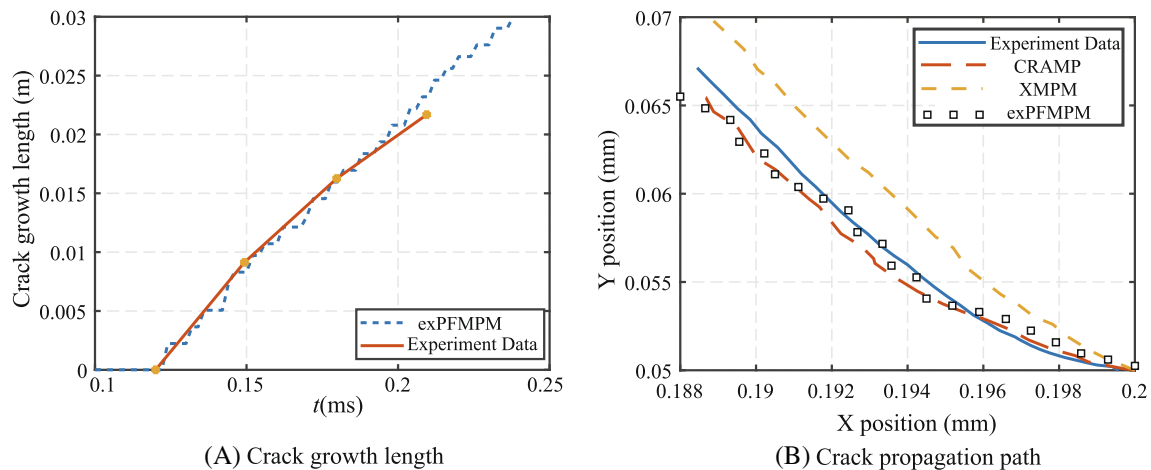

FIGURE 29 Crack growth length and crack propagation path of different solution with $e = 0.1$.

XMPM can accurately capture the crack's initial propagation time which is approximately at $t = 0.16$ ms, but the CRAMP results in a slight delay on the start of crack growth. Furthermore, compared to CRAMP and XMPM, ex-PFMPM has better prediction to the propagation length as shown in Figure 28. Both CRAMP and XMPM overestimate the crack growth length compared to the experimental results, especially in CRAMP.

As shown in Figure 27B–D, the eccentric impact with $e = 0.1, 0.2$, and 0.3 are also simulated using the ex-PFMPM. The eccentric impact will lead to a change in the crack direction towards the impact point. The general direction of all the eccentric impact with $e = 0.1, 0.2$, and 0.3 is similar to that obtained by the experiments. Because Nishioka et al.[50] only gave the experimental data for the eccentric impact with $e = 0.1$, the numerical comparison will only be conducted for this experiment. Figure 29A plots the crack length versus time obtained by the experiment and ex-PFMPM, which show that the ex-PFMPM have good agreement with the experiment. And Figure 29B shows the evolution of the crack propagation paths. Although, the general direction obtained by CRAMP, XMPM, and ex-PFMPM is the same, ex-PFMPM gives better prediction.

5 | CONCLUSION

In this work, we proposed an explicit phase field material point method (ex-PFMPM) for brittle dynamic fracture problems. The rate-independent phase field governing equation is discretized by a set of particles. Based on this idea, the simulation procedure of ex-PFMPM is established, in which the phase field is updated by the explicit forward-difference time integration directly. Furthermore, the stability of ex-PFMPM is studied. A novel 1D 2-cell formula to calculate the critical time step is obtained using the Gerschgorin's theorem, which take the effect of the particle position in the background grids into account. The 1D 2-cell formula can give an underestimated critical time step, which can guarantee the

simulation stability. The 1D 2-cell formula is extended to the 2D and 3D formulae based on the orthogonality of structural Eulerian mesh, which can also be used in the PF-FEM. In the PF-FEM, the currently used estimated formula of the critical time step ignores the effect of the strain energy and may severely overestimate the critical time step, which will lead to instability during the simulation. On the contrary, our formulae can provide a satisfactory estimation for the critical time step in the PF-FEM with single-point Gaussian quadrature and the lumped mass matrix.

The proposed ex-PFMPM is considered to be efficient for the analysis of the dynamic fracture problem, and has the potential to model the dynamic fracture problem with large deformation. A 1D string with pre-existing crack is studied with ex-PFMPM, which indicates that the time step determined by the 2-cell formula is an efficient and relatively accurate estimation of the precise critical time step and is worth employed in numerical applications. To test the ex-PFMPM, three complex numerical examples are studied in this work, including a dynamic crack branching, a plate with pre-existing crack under velocity boundary conditions and a three point bending problem. And the use of the history field in the explicit method is investigated, which shows that it will lead to the fake phase field update and overestimation of the fracture energy in the unloading case. All of the numerical results show that the proposed ex-PFMPM has the capacity of modeling the crack initiation and propagation problems with both accuracy and efficiency. However, the proposed work focus on the dynamic fracture problem in the elastical material. To get a better application prospect, future work in computational modeling of the ex-PFMPM must account for the ductile fracture in the elastoplastic material with large deformation.

DATA AVAILABILITY STATEMENT
Data sharing not applicable to this article as no datasets were generated or analyzed during the current study.

ORCID
Xiong Zhang https://orcid.org/0000-0001-9905-281X
Yan Liu https://orcid.org/0000-0002-6894-9613

REFERENCES
1. Anderson TI. *Fracture Mechanics: Fundamentals and Applications.* CRC; 2005.
2. Sih GC. Numerical analysis of dynamic crack problems. *Elastodynamic Crack Problems.* Noordhoff International Publishing; 1977.
3. Mos N, Dolbow J, Belytschko T. A finite element method for crack growth without remeshing. *Int J Numer Methods Eng.* 1999;46:131-150.
4. Xu XP, Needleman A. Numerical simulations of dynamic interfacial crack growth allowing for crack growth away from the bond line. *Int J Fract.* 1996;74(3):253-275.
5. Carpinteri A, Ferro G, Ventura G. An augmented Lagrangian element-free (ALEF) approach for crack discontinuities. *Comput Methods Appl Mech Eng.* 2001;191(8/10):941-957.
6. Krysl P, Belytschko T. The element free Galerkin method for dynamic propagation of arbitrary 3-D cracks. *Int J Numer Methods Eng.* 1999;44:767-800.
7. Rao BN, Rahman S. Mesh-free analysis of cracks in isotropic functionally graded materials. *Eng Fract Mech.* 2003;70(1):1-27.
8. Rabczuk T, Belytschko T. Cracking particles: a simplified meshfree method for arbitrary evolving cracks. *Int J Numer Methods Eng.* 2004;61(13):2316-2343.
9. Rabczuk T, Zi G, Bordas S, Nguyen-Xuan H. A simple and robust three-dimensional cracking-particle method without enrichment. *Comput Methods Appl Mech Eng.* 2010;199(37-40):2437-2455.
10. Borden MJ, Verhoosel CV, Scott MA, Hughes T, Landis CM. A phase-field description of dynamic brittle fracture. *Comput Methods Appl Mech Eng.* 2012;217-220:77-95.
11. Francfort G, Marigo J. Revisiting brittle fracture as an energy minimization problem. *J Mech Phys Solids.* 1998;46(8):1319-1342.
12. Aldakheel F, Hudobivnik B, Hussein A, Wriggers P. Phase-field modeling of brittle fracture using an efficient virtual element scheme. *Comput Methods Appl Mech Eng.* 2018;341:443-466.
13. Borden MJ, Hughes TJR, Landis CM, Anvari A, Lee IJ. A phase-field formulation for fracture in ductile materials: finite deformation balance law derivation, plastic degradation, and stress triaxiality effects. *Comput Methods Appl Mech Eng.* 2016;312:130-166.
14. Marreddy A, Roland K, Laura DL. A phase-field model for ductile fracture at finite strains and its experimental verification. *Comput Mech.* 2016;57:149-167.
15. Miehe C, Hofacker M, Schanzel LM, Aldakheel F. Phase field modeling of fracture in multi-physics problems. Part II. Coupled brittle-to-ductile failure criteria and crack propagation in thermo-elastic plastic solids. *Comput Methods Appl Mech Eng.* 2015;294:486-522.
16. Li B, Peco C, Millan D, Arias I, Arroyo M. Phase-field modeling and simulation of fracture in brittle materials with strongly anisotropic surface energy. *Int J Numer Methods Eng.* 2014;102(3-4):711-727.
17. Gultekin O, Dal H, Holzapfel GA. Numerical aspects of anisotropic failure in soft biological tissues favor energy-based criteria: a rate-dependent anisotropic crack phase-field model. *Comput Methods Appl Mech Eng.* 2018;331:23-52.

18. Miehe C, Welschinger F, Hofacker M. Thermodynamically consistent phase field models of fracture: Variational principles and multi-field FE implementations. *Int J Numer Methods Eng*. 2010;83:1273-1311.

19. Ren HL, Zhuang XY, Anitescu C, Rabczuk T. An explicit phase field method for brittle dynamic fracture. *Comput Struct*. 2019;217:45-56.

20. Wang T, Ye X, Liu Z, Chu D, Zhuang Z. Modeling the dynamic and quasi-static compression-shear failure of brittle materials by explicit phase field method. *Comput Mech*. 2019;64:1537-1556.

21. Ziaei-Rad V, Shen Y. Massive parallelization of the phase field formulation for crack propagation with time adaptivity. *Comput Methods Appl Mech Eng*. 2016;312:224-253.

22. Sulsky D, Chen Z, Schreyer HL. Particle method for history-dependent materials. *Comput Methods Appl Mech Eng*. 1994;118(1-2):179-196.

23. Zhang X, Chen Z, Liu Y. *The Material Point Method: A Continuum-Based Particle Method for Extreme Loading Cases*. Academic Press; 2016.

24. Nairn JA. Material point method calculations with explicit cracks. *Comput Model Eng Sci*. 2003;4(6):649-664.

25. Wang B, Karuppiah V, Lu H, Komanduri R, Roy S. Two-dimensional mixed mode crack simulation using the material point method. *Mech Compos Mater Struct*. 2005;12(6):14.

26. Chen Z, Feng R, Xin X, Shen L. A computational model for impact failure with shear-induced dilatancy. *Int J Numer Methods Eng*. 2010;56(14):1979-1997.

27. Liang Y, Benedek T, Liu Y, Zhang X. Material point method with enriched shape function for crack problems. *Comput Methods Appl Mech Eng*. 2017;322:541-562.

28. Kakouris E, Triantafyllou S. Phase-field material point method for brittle fracture. *Int J Numer Methods Eng*. 2017;112:1750-1776.

29. Kakouris EG, Triantafyllou SP. Phase-field material point method for dynamic brittle fracture with isotropic and anisotropic surface energy. *Comput Methods Appl Mech Eng*. 2019;357:112503.

30. Cheon Y, Kim H. An adaptive material point method coupled with a phase field fracture model for brittle materials. *Int J Numer Methods Eng*. 2019;120:987-1010.

31. Wolper J, Fang Y, Li M, Lu J, Gao M, Jiang C. CD-MPM: continuum damage material point methods for dynamic fracture animation. *ACM Trans Graph*. 2019;38:1-15.

32. Renaud A, Heuzé T, Stainier L. A discontinuous Galerkin material point method for the solution of impact problems in solid dynamics. *J Comput Phys*. 2018;369:80-102.

33. Renaud A, Heuzé T, Stainier L. Stability properties of the discontinuous Galerkin material point method for hyperbolic problems in one and two space dimensions. *Int J Numer Methods Eng*. 2020;12:664-689.

34. Tran QA, Solowski W. Temporal and null-space filter for the material point method. *Int J Numer Methods Eng*. 2019;120(3):328-360.

35. Belytschko T, Guo Y, Liu WK. A unified stability analysis of meshless particle methods. *Int J Numer Methods Eng*. 2000;48(9):1359-1400.

36. Puso MA, Chen JS, Zywicz E. Meshfree and finite element nodal integration methods. *Int J Numer Methods Eng*. 2008;74(3):416-446.

37. Park CK, Wu CT, Kan CD. On the analysis of dispersion property and stable time step in meshfree method using the generalized meshfree approximation. *Finite Elem Anal Des*. 2011;47(7):683-697.

38. Balsara DS. Von Neumann stability analysis of smoothed particle hydrodynamics–Suggestions for optimal algorithms. *J Comput Phys*. 1995;121(2):357-372.

39. Steffen M, Kirby RM, Berzins M. Decoupling and balancing of space and time errors in the material point method (MPM). *Int J Numer Methods Eng*. 2010;82(10):1207-1243.

40. Berzins M. Nonlinear stability and time step selection for the MPM method. *Comput Partic Mech*. 2018;5(4):455-466.

41. Spigler R, Marco V. Convergence analysis of the semi-implicit Euler method for abstract evolution equations. *Numer Funct Anal Optim*. 1995;5(6):785-803.

42. Ni R, Zhang X. A precise critical time step formula for the explicit material point method. *Int J Numer Methods Eng*. 2020;121:4989-5016.

43. Sharon E, Gross SP, Fineberg J. Local crack branching as a mechanism for instability in dynamic fracture. *Phys Rev Lett*. 1995;74:B06312.

44. Fliss S, Bhat HS, Dmowska R, Rice JR. Fault branching and rupture directivity. *J Geophys Res: Solid Earth*. 2005;110(B6).

45. Belytschko T, Chen H, Xu J, Zi G. Dynamic crack propagation based on loss of hyperbolicity and a new discontinuous enrichment. *Int J Numer Methods Eng*. 2003;58:1873-1905.

46. Silling SA, Askari E. A meshfree method based on the peridynamic model of solid mechanics. *Comput Struct*. 2005;83:1526-1535.

47. Guo YJ, Nairn J. Simulation of dynamic 3D crack propagation within the material point method. *Comput Model Eng Sci*. 2017;113:389-410.

48. Liang Y, Zhang X, Liu Y. Extended material point method for the 3D crack problems. *Int J Numer Methods Eng*. 2021;122:3044-3069.

49. Huang P, Zhang X, Ma S, Huang X. Contact algorithms for the material point method in impact and penetration simulation. *Int J Numer Methods Eng*. 2011;85(4):498-517.

50. Nishioka T, Tokudome H, Kinoshita M. Dynamic fracture path prediction in impact fracture phenomena using moving finite element method based on Delaunay automatic mesh generation. *Int J Solid Struct*. 2001;38:5275-5301.